Measurement of the forward jet cross–section in the low–x_B region at HERA as a signature of BFKL dynamics

Ewelina Maria Łobodzińska

PhD Dissertation
Institute of Nuclear Physics

Kraków, July 1997

Preface

Thesis performed at the INP in Kraków
and at the DESY laboratory in Hamburg
under the supervision of Prof Albert De Roeck
and of Prof Jacek Turnau.

Contents

1 Introduction

The main aim of high-energy physics is the search for fundamental constituents of matter and the nature of interactions between them. Research in this field has been carried out with various kinds of experiments. Scattering experiments turned out to be very successful in unraveling the structure of matter. In these experiments an energetic point–like test particle is scattered on the probe and its angular and energy distributions are measured. In 1911, while bombarding a golden foil with α particles Rutherford observed occasional large–angle scatterings and from this fact he deduced that a compact nucleus lay at the centre of the atom.

More recently, giant particle accelerators have enabled us to probe the structure of nucleon very finely. In mid–1950s elastic scattering of electrons at Stanford showed that the proton is an extended object with dimension of the order of 1 fm. Inelastic scattering of 20 GeV electrons on nucleons in the late 1960s and early 1970s at Stanford established point–like quark constituents of the proton and revealed approximate scaling of the structure functions. In 1975, higher beam energies allowed observations of logarithmic violations of scaling, which was instrumental for the formulation of Quantum Chromodynamics.

In 1992 the electron–proton collider HERA was commissioned at the Deutsches Elektronen–Synchrotron laboratory in Hamburg. With this accelerator, c.m. energies of 300 GeV can be reached compared to 30 GeV in current fixed–target experiments. This results in a vast increase in phase space, physics potential for lepton–nucleon scattering, and resolution of proton constituents (Q^2 rises by a factor of 100).

The HERA experiments, H1 and ZEUS, are therefore exploring a new kinematical region, which was suggested to be sensitive to new dynamic features of QCD. There are several “dedicated” measurements which are aimed at revealing QCD in the region where values of Bjorken x are very low. One of them is the analysis of deep inelastic scattering events containing, in the hadronic final state, a jet – different from the jet resulting from the quark struck by the virtual photon – emitted close to the proton remnant direction. This measurement is designed in such a way that the traditional DGLAP [2] parton evolution is suppressed and the BFKL evolution [4]– expected to become valid in the low–x area – enhanced. Thus, this analysis has a chance to find a distinct signature of BFKL dynamics in the HERA region.

In this thesis we present detailed studies of the forward jet measurement as a possible footprint of the BFKL evolution. We use data collected in 1994 by the H1 experiment.

In Section 2 the deep inelastic scattering process is briefly described and basic kinematical variables are introduced. We show general principles of the quark parton model and explain how it gets improved by Quantum Chromodynamics. Different evolution schemes used to estimate behaviour of parton densities in a proton are also discussed. Section 3 is devoted to BFKL signatures which may be observed in the HERA experiments. In that section the motivation for the forward jet studies are presented. A short description of the Monte Carlo models used in our analysis is given in Section 4. Main information points on HERA and some details about the H1 detector components relevant for our measurement are presented in Section 5. In Section 6 data selection, sources of background and methods of its removal are explained. Jet studies are reported in Section 7. In Section 8 the data correction method used in this analysis, i.e. Bayes unfolding, is explained. We present some tests performed in order to check correctness of this method and comparison of results obtained with this method and with the simple bin-to-bin unfolding. Section 9 is devoted to the presentation of the final results of the forward jet analysis and to the discussion of these results versus predictions of various models. A short summary is given is Section 10.

All information contained in Sections 2 – 5 is based on literature, while the analysis presented in the next sections has been performed by the author.

2 Deep inelastic scattering

In the electron–proton (ep) deep inelastic scattering (DIS) process – schematically shown in Fig.2.1 – the incoming electron couples to the electroweak current J which probes the structure of the proton. The neutral (NC) and charged (CC) components of the current can be distinguished by the final state electron or neutrino, respectively. The virtuality of the exchanged boson Q^2 determines the resolution with which the proton is probed. For Q^2 much larger than proton mass squared (m_p), the proton can be thought of as a group of quasi–free constituents, partons, one of which interacts with the current while the rest (i.e. the proton remnant) moves on unperturbed.

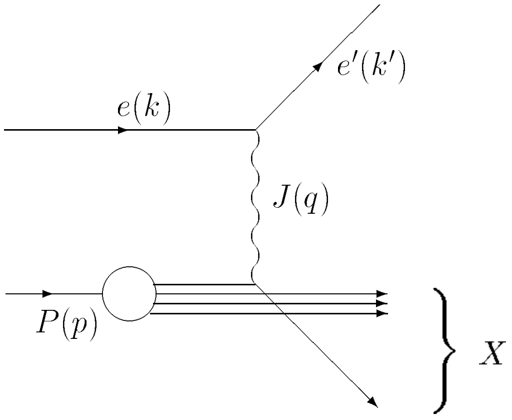

Figure 2.1: *Schematic diagram showing deep inelastic ep scattering as described by the Quark Parton Model.*

Let us label the incoming and the outgoing lepton four–momenta with k and k', respectively, and the proton four–momentum with p. The exchanged boson has four–momentum $q = k-k'$, and the squared centre–of–mass energy of the ep system $s = (k+p)^2$.

For a fixed value of energy $\sqrt{s}$, the inclusive $ep \to eX$ scattering, in which only the scattered electron is measured, is fully described by any two of the following variables:

- $Q^2 \equiv -q^2 = -(k-k')^2 > 0$ – square of the four–momentum transfer,
- $\nu = q \cdot p/m_p$ – energy of the current J in the rest frame of the incoming proton,
- $y = p \cdot q/p \cdot k = \nu/\nu_{max}$ – fraction of the incident electron energy transferred to the proton in the rest frame of the proton.
- $x = Q^2/(2q \cdot p) = Q^2/(2m_p\nu)$ – the Bjorken scaling variable; in the parton model of a deep inelastic collision, it represents the fraction of the proton momentum carried by the struck quark,
- $W^2 = (p+q)^2 = m_p^2 + Q^2(1/x - 1)$ – squared invariant mass of the final hadronic system X.

Three of these variables are related[1] by:

$$xys = Q^2 \ , \tag{2.1}$$

Since both variables, x and y, are bounded by the kinematical condition $0 < x, y < 1$, the maximum value of the momentum transfer is $Q^2_{max} = s$.

Choosing x and Q^2 as independent variables, the differential cross–section for inelastic $ep \rightarrow eX$ scattering has the form:

$$\frac{d^2\sigma}{dxdQ^2} = \frac{4\pi\alpha^2}{xQ^4}[y^2xF_1(x,Q^2) + (1-y)F_2(x,Q^2)], \tag{2.2}$$

where F_1 and F_2 are structure functions of the proton. The $1/Q^4$ dependence results from virtual photon exchange.

In the Bjorken limit, i.e. Q^2 and $2p \cdot q \rightarrow \infty$ while x is fixed, structure functions depend approximately only on dimensionless variable x:

$$F_i(x,Q^2) \approx F_i(x) \ . \tag{2.3}$$

This is the famous Bjorken scaling, first observed in the DIS experiments at SLAC, which finds natural explanation in the quark parton model.

2.1 The quark parton model

While describing deep inelastic electron–proton scattering in the quark parton model (QPM) [1] it is important to refer to a particular frame, called the infinite momentum frame. In this frame the proton is moving very fast so that the relativistic time dilation slows down the rate with which the partons interact with each other. That makes characteristic time of the interaction between the virtual photon and a parton ($1/Q$) much smaller than the time of parton–parton interactions. Thus, one may view the photon as being absorbed *instantaneously* by some quark in the proton and – in other words – the struck quark appears essentially *free* during the short time of interaction with the virtual photon.

Therefore, the electron–proton scattering may be written as an incoherent sum of probabilities of scattering from single free quarks:

$$\frac{d^2\sigma}{dxdQ^2} = \sum_q \int_0^1 d(\xi) f_q(\xi) \left(\frac{d^2\sigma}{dxdQ^2}\right)_{eq} , \tag{2.4}$$

where $f_q(\xi)$ is the probability of finding parton q in the proton carrying fraction ξ of its momentum.

The scattered and unscattered partons recombine then to form hadrons. Hadronization takes place over a long time scale in comparison with the scattering process, so it can be treated separately.

---

[1] High energy limit $s \gg m_P^2$ is assumed.

In the QPM both proton and partons are assumed to be massless in the high energy limit. In this case, fraction ξ of the proton momentum carried by the struck quark is equal to the Bjorken variable x, since the massless condition for the scattered quark gives:

$$0 = (\xi p + q)^2 \qquad \Rightarrow \qquad \xi = \frac{-q^2}{2p \cdot q} = x \ . \tag{2.5}$$

The differential electron–parton cross–section in (2.4) depends on the assumptions about parton structure. Identifying the partons with quarks, spin–1/2 constituents of proton, the elementary cross–section is of the form:

$$\left(\frac{d^2\sigma}{dxdQ^2}\right)_{eq} = \frac{2\pi\alpha_{em}^2 e_q^2}{Q^4}\left[1 + (1-y)^2\right]\delta(x-\xi), \tag{2.6}$$

where α_{em} is the fine structure constant and e_q are fractional charges of quarks. Let us stress that in this case quarks are elementary (pointlike) particles.

Upon inserting equation (2.6) into (2.4) and comparing it with (2.2), one can obtain the following QPM prediction:

$$F_2(x) = 2xF_1(x) = x\sum_q e_q^2 \int_0^1 d\xi f_q(\xi)\delta(x-\xi) = \sum_q e_q^2 x f_q(x). \tag{2.7}$$

This expression displays three important results:

- Structure functions of the proton directly "measure" partonic distributions $f_q(x)$.
- Proton structure functions exhibit the Bjorken scaling (F_2 does not depend on Q^2). This is the result of pointlike structure of quarks.
- Structure functions are not independent: $F_2 = 2xF_1$. This is known as the Callan–Gross relation which follows from the spin–1/2 nature of the charge–carrying constituents of the proton.

The Bjorken scaling is observed for values of $x \sim 0.1$, and the structure functions increase and decrease logarithmically in Q^2 for smaller and larger values of x, respectively. This profound experimental fact, which cannot be accounted for by the QPM, is explained by Quantum Chromodynamics (QCD), the fundamental theory of strong interactions.

2.2 QCD–improved parton model

One of the most crucial features of QCD is dependence of the strong coupling constant α_s on Q^2:

$$\alpha_s(Q^2) = \frac{\alpha_s(\mu^2)}{1 + [\alpha_s(\mu^2)/6\pi](33/2 - n_f)log(Q^2/\mu^2)}, \tag{2.8}$$

where n_f is the number of flavours and μ^2 is an arbitrary normalization point at which the coupling α_s has been measured. In contrast to the QED coupling constant, the QCD coupling $\alpha_s(Q^2)$ decreases with increasing Q^2. This leads to the fact that QCD is asymptotically free, that is $\alpha_s \to 0$ as $Q^2 \to \infty$. This phenomenon, called asymptotic freedom, puts the QPM on a sound theoretical basis, since deep inelastic scattering is a high Q^2 process.

Perturbative QCD can be used to calculate the Q^2 dependence of the deep inelastic structure functions of the proton.

The QPM formula (2.7) may be regarded as the zeroth–order term in the QCD perturbative expansion of the proton structure function. In the first–order approximation one has to add contribution from the processes schematically shown in Fig.2.2(b). After summing the infinite number of such emissions, structure function F_2 takes the following form:

$$F_2(x, Q^2) = \sum_{i=q,\bar{q}} e_i^2 x f_i(x, Q^2) \tag{2.9}$$

where f_i are Q^2–dependent **quark** and **antiquark** distributions in proton.

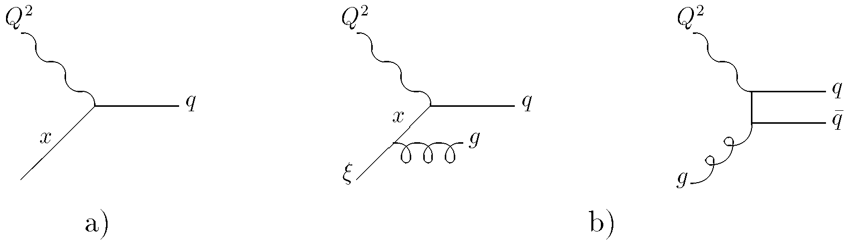

Figure 2.2: *Schematic diagrams of partonic subprocesses contributing to deep inelastic scattering: a) term of the zeroth order in α_s – the QPM, b) terms of the first order in α_s.*

QCD emissions described above lead to the Altarelli–Parisi (DGLAP) evolution equations [2]:

$$\frac{\partial f_i(x, Q^2)}{\partial \log Q^2} = \frac{\alpha_s(Q^2)}{2\pi} \sum_{j=q,\bar{q},g} \int_x^1 \frac{d\xi}{\xi} \, f_j(\xi, Q^2) \; P_{ij}(\frac{x}{\xi}) \; , \tag{2.10}$$

which determine how quark, antiquark and **gluon** distributions evolve with Q^2 once they are known at some initial scale Q_0^2. Functions P_{ij} describe probability of finding parton i with momentum fraction x inside parton j with momentum fraction ξ. Parton distributions are universal, which means that they describe quark (or gluon) composition of the proton in any hard interaction it undergoes.

Perturbative QCD cannot provide initial conditions, i.e. parton distributions at some initial scale Q_0^2, for integration of the DGLAP evolution equations. These have to be taken from DIS experiments. The basic procedure is to parametrize the x dependence of initial densities $f_i(x, Q^2)$ at some low scale Q_0^2 (but high enough to justify the use of perturbative QCD), and then evolve the initial distributions up in Q^2 to compute the cross–sections or structure functions at measured (x, Q^2) points. The initial parameters are tuned to get the best agreement between the computed and the measured quantities.

In this way, the QCD parton model has introduced a definite pattern of scaling violations. Structure functions $F_i(x, Q^2)$ are no longer simply scaling functions of x alone, but have acquired a logarithmic dependence on Q^2.

2.3 Altarelli–Parisi evolution equations

As already mentioned in the previous section, the traditional way to estimate the behaviour of parton densities in a proton is based on the Altarelli–Parisi (also called DGLAP, i.e. Dokshitzer–Gribov–Lipatov–Altarelli–Parisi) evolution equations [2], which in the lowest order resum the leading powers of $\log Q^2$. That is, for each additional factor of α_s only the leading $\log Q^2$ terms accompanying this α_s are kept.

As it was noticed by Dokshitzer [3], in an axial gauge[2] these leading logarithms are generated by "ladder" diagrams of the type shown in Fig.2.3. The diagram with n gluon rungs corresponds to the $(\alpha_s \log Q^2)^n$ contribution. In the DGLAP scheme this parton cascade follows strong ordering in the transverse momenta:

$$Q^2 \gg k_{nT}^2 \gg k_{n-1T}^2 \gg \cdots \gg k_{1T}^2 \tag{2.11}$$

and ordering in the longitudinal momenta:

$$x_n < x_{n-1} < \cdots < x_1 < 1. \tag{2.12}$$

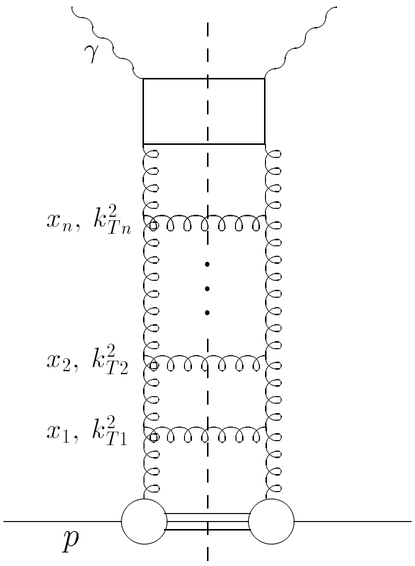

Figure 2.3: *"n–rung" ladder diagrams which are effectively resummed by the DGLAP and BFKL evolution equations.*

2.4 Evolution equations in the low–x region

When x is small, the partons are mainly gluons, so attention is focused on the evolution of gluon densities $g(x, Q^2)$ in a proton. In the low–x and large Q^2 region, behaviour

---

[2] An axial gauge is one in which the gluon has only two physical polarization states; in such a gauge we do not need unphysical "ghosts" contributions which in general would be required to cancel the scalar polarization component of the gluon.

of $g(x,Q^2)$ can be calculated in the double leading logarithmic approximation (DLLA) of the DGLAP equations. This involves summation of the double leading logarithmic contributions proportional to $(\alpha_s \log Q^2 \log 1/x)^n$. It amounts to resummation of the ladder diagrams where both the transverse and fractional longitudinal gluon momenta are strongly ordered along the ladder (Fig.2.3):

$$Q^2 \gg k_{nT}^2 \gg k_{n-1T}^2 \gg \cdots \gg k_{0T}^2 \tag{2.13}$$

$$x_n \ll x_{n-1} \ll \cdots \ll x_1 \tag{2.14}$$

The sum of these graphs gives, up to slowly varying logarithmic factors, the following formula:

$$xg(x,Q^2) \sim exp\left[2\left(\frac{3\alpha_s}{\pi}\log(Q^2)\log\left(\frac{1}{x}\right)\right)^{\frac{1}{2}}\right] \tag{2.15}$$

However, this approximation does not take into account all leading terms in the small–x limit. Terms containing the leading power of $\log(1/x)$, but not accompanied by the leading powers of $\log Q^2$, are neglected. So, if we are interested in small x but moderate Q^2 values, the BFKL (Balitsky-Fadin-Kuraev-Lipatov) equation [4] is more appropriate. It sums leading $\alpha_s \log 1/x$ terms and keeps the full Q^2 dependence. The strong ordering in transverse momenta required by the DGLAP evolution equations is now relaxed and the integration is carried over the full k_T phase–space. This equation is also identified with summation of the ladder diagrams shown in Fig.2.3, but now the gluon cascade follows strong ordering in fractional longitudinal momenta:

$$x_n \ll x_{n-1} \ll \cdots \ll x_1 \tag{2.16}$$

The sum of these diagrams leads to a low–x gluon density behaviour of the form :

$$xg(x,Q^2) \sim x^{-\alpha_p+1} \tag{2.17}$$

with $\alpha_p - 1 = (12\alpha_s)/\pi \log 2$, where α_p is the intercept of the trajectory of the so–called Lipatov Pomeron. In the above, effects of the running α_s and of slowly varying logarithmic factors are omitted. For a typical value of $\alpha_s \approx 0.2$, we have $\alpha_p - 1 \approx 0.5$, so the strong rise of $xg(x,Q^2)$ should be observed for $x \to 0$.

The three different limits of $g(x,Q^2)$ in the ($\log Q^2$, $\log 1/x$) plane are shown in Fig.2.4:

- **the leading** $log(Q^2)$ **region**: $\log Q2/Q_0^2 \gg 1$, $\log 1/x \sim 1$, parton densities are described by the Altarelli–Parisi evolution equations,
- **the double leading log region**: $\log Q_2/Q_0^2 \gg 1$, $\log 1/x \gg 1$, parton densities are described by the Altarelli–Parisi evolution, where only terms proportional to $(\alpha_s \log(Q^2)\log(1/x))^n$ are kept,
- **the leading** $log(1/x)$ **region**: $\log Q^2/Q_0^2 \sim 1$, $log 1/x \gg 1$, parton densities are described by the BFKL evolution equation.

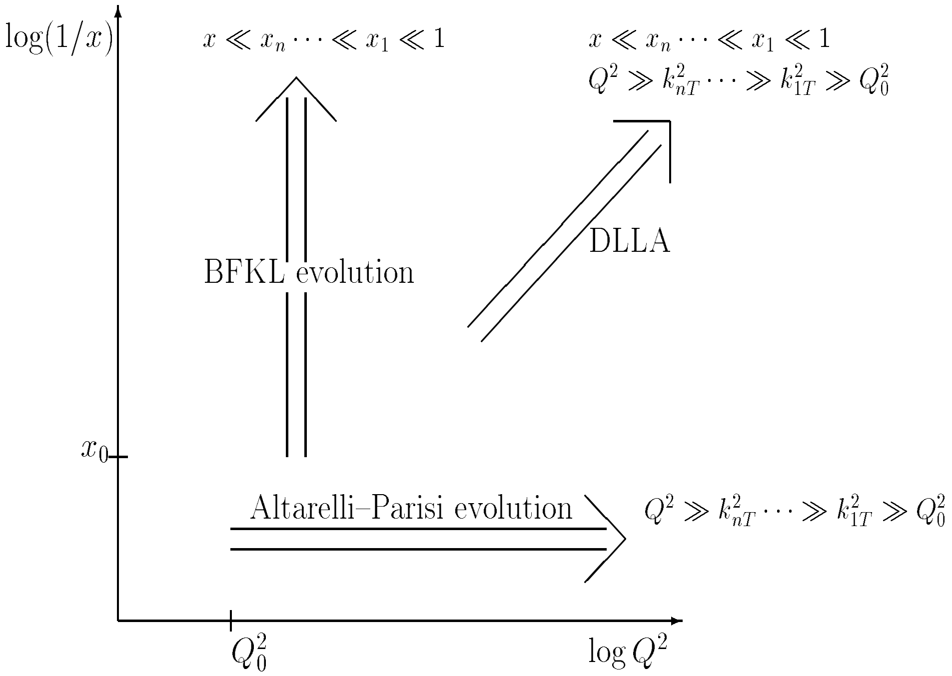

Figure 2.4: *Three limits of* $g(x,Q^2)$ *in the* $(\log(Q^2), \log(1/x))$ *plane.*

3 Possible BFKL signatures in the low–x region at HERA

The $e-p$ collider HERA entered a new kinematical region, where values of the Bjorken variable x_B are very small (10^{-2} – 10^{-4}) and virtuality Q^2 is large enough to justify the use of perturbative QCD, so one can expect that the effects predicted by the BFKL evolution equation may occur.

The proton structure function F_2, measured by two HERA experiments, H1 and ZEUS, really exhibits a steep growth with decreasing x_B [5] (Fig.3.1).

In this figure, experimental data are compared with various theoretical predictions, in particular with the MRS(D0) curve based on traditional scenarios without the Lipatov Pomeron and computed when no HERA data were available, and also with the MRS(D-) curve calculated with the assumption that gluon density for low–x is proportional to $x^{-0.5}$. It turned out that real data agree with neither of these extreme approximations but lie inbetween.

This behaviour of F_2 caused a heated debate on whether the HERA data are still in a region where the QCD evolution of gluon densities can be described by the DGLAP evolution equations, or whether they extend into a new region where QCD dynamics is described by the BFKL evolution equation. The final conclusion seems to be that present F_2 measurements do not yet allow us to discriminate between these two evolution schemes, and therefore other less inclusive measurements are necessary.

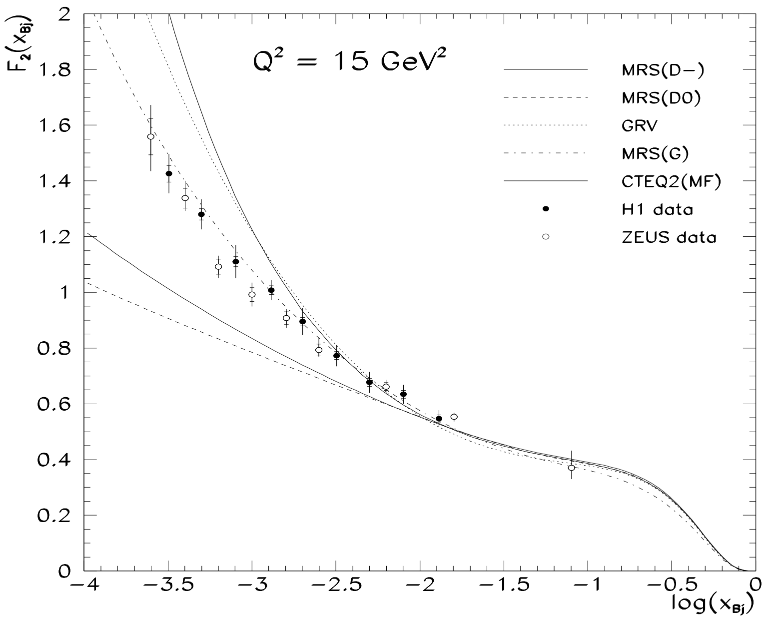

Figure 3.1: *F_2 proton structure function as measured by the HERA experiments in 1994.*

One of the simplest observables suggested as a test of the BFKL versus DGLAP hypothesis is the flow of transverse energy (E_T) as a function of rapidity η in the hadronic centre–of–mass frame.[3]

BFKL calculations [6] predict an increase of mean transverse energy $\langle E_T \rangle$ with decreasing x_B, while DGLAP calculations predict just the opposite. In addition, due to transverse momentum ordering, the DGLAP evolution is expected to produce less E_T in the region between the current and the remnant jets for low–x_B events, as compared to the BFKL evolution [6].

Analysis of transverse energy flow based on the H1 data collected in 1993 has produced very promising results. The E_T flow in the CMS as a function of rapidity has been reasonably well described by CDM Monte Carlo model (in this model gluons in the ladder are not ordered in transverse momenta, so it is sometimes called the BFKL–like model) in all x_B and Q^2 bins, while the MEPS Monte Carlo model (DGLAP–based model)[4] has followed the data for large x_B and Q^2 values only.

However, it appears that the recently improved version of the DGLAP–based model[5] provides a good overall description of the measured transverse energy flow. Also the $\langle E_T \rangle$ distribution is now fairly well described by both Monte Carlo models.

Nevertheless, the model based on the DGLAP evolution scheme needs to produce 60-80% of its transverse energy during the hadronization phase so as to be able to follow the data. Hadronization allows it not only to increase the amount of E_T significantly, but even to compensate for the wrong x_B dependence seen at the parton level.

---

[3] Particle masses are neglected so that rapidity is equal to pseudorapidity $\eta = -\ln \tan \Theta/2$.

[4] CDM – Colour Dipole Model, MEPS – Matrix Elements + Parton Shower. Monte Carlo models will be described in detail in the next chapter.

[5] Soft colour interactions were added and the sea–quark (remnant) treatment was improved.

Since analysis of transverse energy flow also turned out to be inconclusive, more attention has been paid to other possible signatures of BFKL dynamics, such as:

- Measurement of charged particles p_T spectra [7]. This measurement is not so sensitive to hadronization effects, so hard tails of the p_T distributions, as seen in the data, are well described by the CDM Monte Carlo model, while the MEPS model predicts much softer spectra.
- Di–jet production. It was suggested [8] that weakening of the azimuthal (back-to-back) correlation between jets produced in DIS at HERA may be used to identify BFKL dynamics. From the experimental point of view, such analysis seems to be quite difficult; nevertheless, serious attempts to test this effect have been made.
- Forward jet production [9], [10, 11], [12].
- Azimuthal decorrelation of the forward jet [13].

The last two items will be covered here since detailed analysis of the forward jets as a potential footprint of BFKL dynamics constitues the principal topic of this thesis.

3.1 Forward jets as a signature of BFKL dynamics at HERA region

A proposal of a measurement which would be able to probe the low–x region was made by Mueller [9] and thoroughly examined by the Durham [10, 11] and DESY [12] groups. The idea is to study deep inelastic scattering events containing, in a hadronic final state, a jet characterized by fractional longitudinal momentum $x_{jet} = p_{z_{jet}}/p$ (where p is proton momentum and $p_{z_{jet}}$ is longitudinal jet momentum) and transverse momentum $k_{T_{jet}}$ (Fig.3.2). Such events will be referred to as (DIS +) forward jet events.

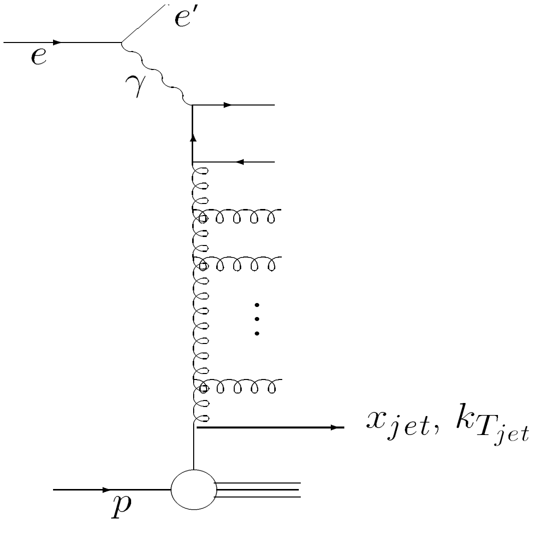

Figure 3.2: *Schematic diagram of deep inelastic scattering events containing, in a hadronic final state, a forward jet that arises from either a quark or a gluon.*

In order to focus on the BFKL type of evolution, the two basic conditions have to be met:

- $k^2_{T_{jet}} \sim Q^2$
- $x_{jet} \gg x_B$

The former ensures suppression of the DGLAP type of evolution, since it leaves no room for strong ordering in transverse momenta. The latter requirement maximizes phase–space for the BFKL evolution.

As seen in Fig.3.2 the jet under consideration – in order to fulfill the second condition – is emitted close to the proton remnant direction defined as the forward direction in the HERA geometry.

The diagram relevant to the computation of the cross–section for the process illustrated in Fig.3.2 is shown below (Fig.3.3).

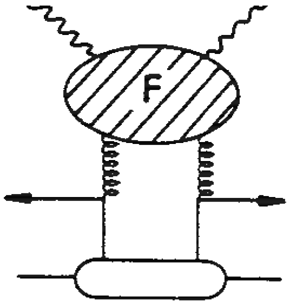

Figure 3.3: *Diagram illustrating the terms used for computation of the cross–section for the DIS + jet production process. The figure is taken from [11].*

F denotes the photon–gluon subprocess which embodies all the BFKL emissions and formally satisfies the BFKL equation,

$$F(z,Q^2,k_T^2) = F_0(k_T^2) + \int_z^1 \frac{dz'}{z'} \int dk_T'^2 K(k_T,k_T')F(z',Q^2,k_T'^2), \quad z = x_B/x_{jet} \tag{3.1}$$

which is symbolically shown in Fig.3.4.

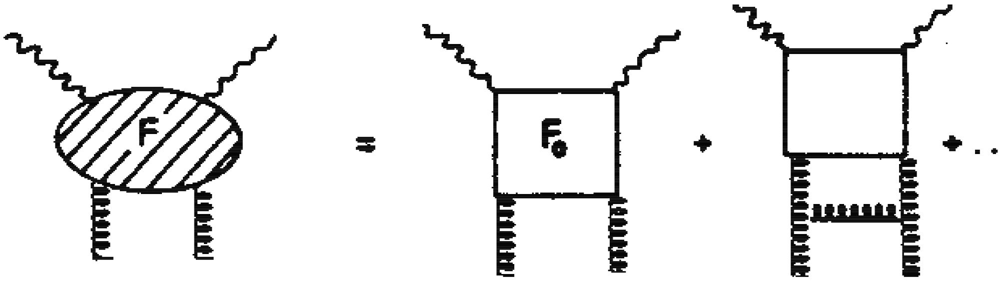

Figure 3.4: *Leading log$(1/x)$ approximation for F. The figure is taken from [11].*

F_0 is just the quark box (and the crossed quark box), i.e. the contribution where no gluon is emitted in the ladder – **the Born approximation**. The remaining term effectively sums the gluon ladder contribution arising from both virtual and real gluon emissions.

Since the photon is probing the parton (which produces a jet) rather than the proton itself, and the jet is expected to have quite large x_{jet}, we only need to provide parton distributions in the region where they are well known. This way the problem of having to provide parton distributions at small x is avoided. In terms of the jet variables the differential deep inelastic structure function has the form:

$$\frac{\partial F_2}{\partial x_{jet} \partial k_T^2} = \frac{3\alpha_s(Q^2)}{\pi k_T^4} \sum_a f_a(x_{jet}, k_T^2) F(z, Q^2, k_T^2) \tag{3.2}$$

where f_a denotes parton distributions.

Equations 3.1 and 3.2 are used to evaluate the differential cross–section for production of deep–inelastic + forward jet events. Calculations are done in two ways:

1. Only for the box diagram ($F = F_0$), so we get the cross–section without the BFKL effects. This is the Born approximation for the forward jet process.
2. Taking into account gluon emissions. Assuming the running coupling constant, equation 3.1 may be solved numerically by evolving down in z, starting at the boundary condition $F = F_0$ at some value of z_0 where the BFKL effect is expected to be small.
   Cross–section obtained in this way exhibits a steep rise with decreasing z.

Calculations results constitute the main motivation for the forward jet analysis and will be compared with the DIS + forward jet cross–section measured in the data.

In the end, let us stress again the ingenuity of Mueller's idea. In the forward jet measurement, phase–space for the BFKL type of evolution is maximized by the condition $x_{jet} \gg x_B$, and at the same time the DGLAP parton emissions are suppressed by the requirement $k_T^2 \sim Q^2$. Thus, this measurement has a chance to provide a distinct footprint of BFKL dynamics.

3.2 Azimuthal dependence of forward jets

Analysis of azimuthal dependence of forward jets was proposed [13] as a further signal of BFKL dynamics. In HERA reference frame, BFKL dynamics predicts that with increasing rapidity difference between the forward and the current jets, the forward jet "forgets" about the azimuthal direction defined by the outgoing electron, so the cross–section becomes $\Delta\phi$–independent. $\Delta\phi$ is defined in the HERA frame as the angle between transverse momenta of the outgoing lepton and the forward jet.

Azimuthal dependence of the forward jet production cross–section was calculated in [13] assuming the BFKL gluon evolution in the ladder. The result may be expressed by the following formula:

$$\frac{d\sigma}{d\Delta\phi} \sim A + C\cos(2\Delta\phi). \tag{3.3}$$

Coefficient C is negative, so at $\Delta\phi = \pi/2$ there is a maximum. However, with increasing x_{jet}/x_B the angular dependent part is suppressed while A increases. This confirms our expectations of the BFKL prediction to be $\Delta\phi$–independent for low–x_B.

Fig.3.5 shows prediction of azimuthal dependence for the Born and BFKL cases (plot on the left-hand-side). The Born calculations give only approximate predictions, so the results of the fixed–order matrix element numerical studies for various x_B ranges are also presented (the right-hand-side plot). For numerical calculations, the PROJET [14] Monte Carlo is used with the matrix element $g \to qq'g$, integrated over the full range of invariant mass squared $s_{q\bar{q}}$, where any of the partons may initiate the forward jet.

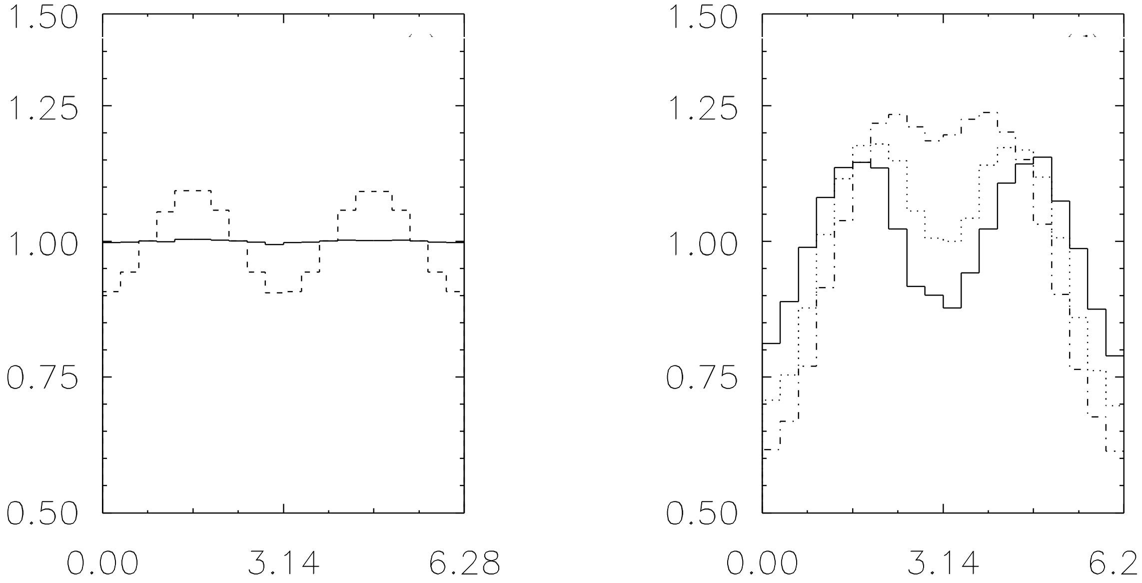

Figure 3.5: *Dependence on the difference in azimuthal angles of the outgoing electron and the forward jet, normalized to a common average. The left-hand figure: solid line – the BFKL result, dashed line – the approximative analytical Born prediction;* $0.2\cdot10^{-3} < x_B < 0.4\cdot10^{-3}$ *. The right-hand figure: fixed-order results,* $0.2\cdot10^{-3} < x_B < 0.4\cdot10^{-3}$ *– solid line,* $1.8\cdot10^{-3} < x_B < 2.\cdot10^{-3}$ *– dotted line,* $3.4\cdot10^{-3} < x_B < 3.6\cdot10^{-4}$ *– dashed–dotted line.*

One may see that for the approximate analytical Born result the cross–section has a clear maximum at $\Delta\phi = \pi/2$. For the fixed–order results this cosine–like structure is deformed, as the maximum moves towards $\Delta\phi = \pi$. However, the biggest discrepancies between the numerical and Born predictions are observed for high values of x_B. In the BFKL case, any $\Delta\phi$–dependence is completely washed out.

In the analysis of the DIS + forward jet events we will also concentrate on the correlation in the azimuthal angle between the forward jet and the outgoing electron. Predictions of this section will be used for interpretation of our measurement results.

4 DIS Monte Carlo models

For comparison of the measurements with QCD predictions, models which describe the QCD processes at the parton level and the fragmentation into hadrons are indispensable.

In the H1 collaboration the Monte Carlo production is performed in three steps:

1. Event generation
   Various models generating ep scattering events are available. They differ mainly in the details of the parton cascade simulation and the phenomenological description of hadronization. Monte Carlo models considered in the analysis of the forward jet production are shortly described in the next section.

2. Detailed simulation of the H1 detector response
   Final state particles produced by Monte Carlo generators are traced through the H1 detector by means of the H1 simulation program – H1SIM. H1SIM works within the GEANT [21] frame and simulates responses of each part of the H1 detector.

3. Reconstruction of the simulated events
   Simulated events are reconstructed in the same way as the real data. For this purpose, the H1REC package is used.

In the following we describe MC programs used in this analysis.

LEPTO

In LEPTO [15] QCD processes are calculated up to $O(\alpha_s)$ according to exact first order matrix elements (ME). It contains the following processes:

- the leading–order parton–level process, $\gamma q \to q$ — shown by the diagram of the naive quark–parton model (QPM) in Fig.4.1 (a),
- gluon radiation (QCD–Compton), $\gamma q \to qg$ – Fig.4.1 (b),
- boson–gluon fusion (BGF), $\gamma g \to qq$ – Fig.4.1 (c).

Higher order contributions are simulated in the leading logarithmic approximation by the parton shower (PS).

In DIS the quark struck by the electroweak boson can emit partons either before or after the boson vertex giving rise to initial and final parton showers, respectively.

A parton in the incoming nucleon and close to the mass–shell can initiate a parton emission cascade. In each branching of the cascade, the parton becomes more off–shell with a space–like virtuality ($m^2 > 0$) due to radiation of on–shell or having a time–like virtuality ($m^2 < 0$) parton.

This initial state space–like shower results in a space–like quark which interacts with the electroweak boson that turns it into an outgoing quark which is either on–shell or has a time–like virtuality. In the latter case a final state time–like shower will result. Off–shell mass is reduced by branching into daughter partons with decreasing off–shell masses and decreasing opening angles. This shower continues until all partons are (essentially) on–shell. Any parton with a time–like virtuality from the initial state shower will develop similarly. General behaviours of initial and final state parton showers are similar since

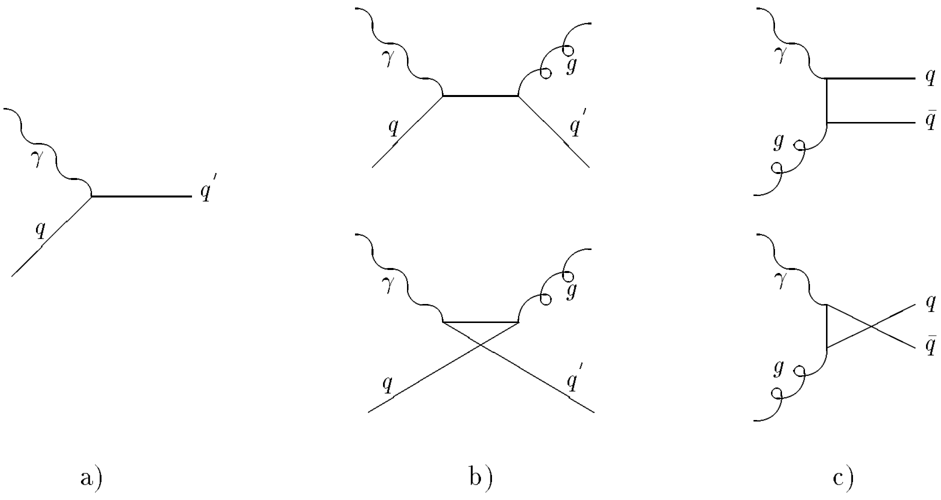

Figure 4.1: *Basic parton processes implemented in LEPTO:*
a) diagram of naive quark–parton model,
b) diagrams contributing to the QCD–Compton process,
c) diagrams contributing to the BGF process.

they are both based on branching processes: $q \rightarrow qg$, $g \rightarrow q\bar{q}$, $g \rightarrow gg$ as described by the Altarelli–Parisi evolution equations in the leading logarithmic approximation of the QCD.

Combination of the two approaches (ME+PS) gives the first order parton emission plus the higher–order emissions through parton shower.

Fragmentation into hadrons is performed with the Lund string model as implemented in JETSET [20].

ARIADNE – CDM

ARIADNE [18] is a generator for QCD cascades only. Gluon radiation is performed in Ariadne by implementation of the Colour Dipole Model (CDM). In contrast to the bremsstrahlung–like parton shower model, the CDM model does not distinguish between initial and final state radiation and includes interference effects between them. The struck parton and the proton remnant form a colour dipole. When this dipole radiates a gluon, it splits into two radiating dipoles: one between the struck quark and the emitted gluon, and another one between the emitted gluon and the remnant. Further gluon radiations lead to a chain of such dipoles.

The CDM model, in contrast to LEPTO and HERWIG which are based on DGLAP evolution equation, is called BFKL–like model because gluons emitted in the cascade do not obey strong ordering in k_T.

DJANGO

The event generator DJANGO [16] simulates deep inelastic lepton–proton scattering. It includes both QED and QCD radiative effects and allows for generation of events according to QCD cascade models or QCD matrix elements. These are matrix elements available which describe effects from perturbative QCD to first order in α_s due to virtual gluon emission and boson–gluon fusion. A combination of LLA QCD cascades with first–order matrix elements is possible. QCD cascades can be generated using either the parton shower (PS) model implemented in LEPTO, or the colour dipole model as implemented in ARIADNE [18].

Process $ep \rightarrow e'X$, including electroweak corrections of $O(\alpha)$ and the bremsstrahlung process $ep \rightarrow e'\gamma X$, is simulated with the help of HERACLES [17]. The full hadronic final state is generated using the Lund string model JETSET [20].

JETSET

The JETSET [20] Monte Carlo program is a generic package for jet fragmentation, particle decays, final–state parton showers, event–analysis routines, and other utilities.

Many Monte Carlo programs that generate parton configurations in different processes use JETSET for fragmentation. The fragmentation in JETSET is based on a string fragmentation model.

In the string model a string is stretched between colour–connected partons, so as to make colour singlet strings of minimum invariant mass. The string has a uniform energy per unit length, corresponding to a linear quark confining potential. Gluons are supposed to produce kinks on the string, each initially carrying localized energy and momentum equal to that of its parent gluon. The string breaks up into hadron–sized pieces through spontaneous $q\bar{q}$ pair production in its intense colour field. The string break–up process proceeds until only on–mass–shell hadrons remain.

A large fraction of the particles produced by fragmentation are unstable and subsequently decay into stable ones. The decay treatment is handled by JETSET, making use of a set of tables where branching ratios and decay modes are stored.

5 Experimental apparatus

5.1 HERA collider

Traditionally, lepton–nucleon interactions were investigated in fixed–target experiments where a stationary target was hit by a beam of high energy leptons. Colliding–beam accelerators allowed the energy accessible in the c.m. frame to be significantly increased as compared to fixed–target experiments. The electron–proton collider differs from electron–electron or proton–proton colliders mainly by the fact that it needs two independent magnet rings and accelerating systems. Electrons and protons have to be stored in two separate rings due to a big mass difference. Since electrons have small masses, energy loss by synchrotron radiation is very large ($\sim 1/\mathrm{m}_e^4$), and thus the electron beam needs much more power pumped in so as to compensate for the losses, which in consequence limits the practical energy achievable. Due to their bigger masses, protons may be accelerated to higher energies, but then stronger magnetic field is needed to keep them in the orbit. This leads to the fact that, in contrast to the electron ring, the proton one has to be equipped with superconducting magnets.

Hadron–Electron Ring Accelerator (HERA) is the first and only electron–proton collider. It was commissioned at the Deutsches Elektronen–Synchrotron (DESY) laboratory in Hamburg, Germany in 1992. HERA consists of two independent accelerators designed to store 820 GeV protons and 30 GeV electrons and to collide them head–on at four interaction points spaced uniformly around its 6.3 km – long underground tunnel. At present two multipurpose detectors are running at two of the interaction points – the H1 detector situated in the North Hall and the ZEUS detector in the South Hall.

At the beginning of 1994 HERA operated with $\mathrm{e}^-\mathrm{p}$ collisions, later the electron beam was replaced with a positron one[6]. The positron beam shows much better stability and is easier to guide than the electron one. Lifetime of the electron ring fills is almost 2 times higher for the positron than for the electron beams.

Integrated luminosity for physics analysis was 0.4 pb^{-1} for e^-p and 2.7 pb^{-1} for e^+p . The electron and proton beams were organized into 168 and 170 bunches, respectively. 153 bunches were colliding, separated from each other by 96 ns.

A summary of parameters designed and achieved in 1994 at the HERA collider is shown in Table 5.1.

5.2 H1 detector

The H1 detector is a nearly hermetic multi–purpose apparatus built to investigate inelastic high–energy interactions of electrons and protons at HERA. The H1 coordinate system is defined in such a way that its origin is placed at the nominal interaction point. Initial protons move in the positive z direction, the x coordinate points towards the centre of the HERA ring, and the y coordinate points upwards. Polar angle Θ is defined with respect to the proton beam direction.

The H1 detector is asymmetric. Asymmetry is required by the HERA event topology because the centre of mass of the collision is strongly boosted along the proton beam

---

[6] In this thesis the incident and scattered lepton will always be referred to as an electron.

HERA parameters	designed		running in 1994	
	electron	proton	electron	proton
Nominal Energy (GeV)	30	820	27.6	820
C.M. Energy (GeV)	314		301	
Maximum Q^2 (GeV^2)	9×10^4		9×10^4	
Luminosity (cm^{-2}s^{-1})	1.5×10^{31}		0.5×10^{31}	
Circumference (m)	6336			
Injection Energy (GeV)	14	40	14	40
Circulating Current (mA)	58	163	5 – 30	10 – 50
Number of Bunches	210		153	
Time between Crossings (ns)	96		96	
Horizontal Beam Size σ_x (mm)	0.26	0.29	0.27	0.18
Vertical Beam Size σ_y (mm)	0.07	0.07	0.06	0.06
Longitudinal Beam Size σ_z (cm)	0.8	11	0.8	11

Table 5.1: *Design and 1994–running values of the main HERA parameters.*

direction, and consequently high densities of energetic particles are expected in the forward region.

All *ep* collisions occur in the interaction region, the longitudinal dimension of which is determined by the length of the proton bunch and was found in 1994 to be $\sigma_{zvtx} = 11\ cm$.

General layout of the detector is shown in Fig.5.1. The interaction region is surrounded with tracking devices $\boxed{2,3}$ which measure momenta of charged particles and reconstruct the position of the interaction point. The tracking system consists of drift chambers interleaved with proportional chambers which enable fast trigger selection. All detectors are enclosed in calorimeter $\boxed{4,5}$ which permits to measure the energy and direction of charged and neutral particles. The liquid argon calorimeter covers central and forward regions. The very forward direction around the beam pipe is closed by plug calorimeter $\boxed{13}$ constructed of copper absorber and silicon pad readout. The calorimetric coverage in the backward region is completed with electromagnetic calorimeter $\boxed{12}$ located after proportional chamber (BPC)[7] and before two scintillator walls – time–of–flight detectors (TOF) – used to veto proton–induced background events. Superconducting coil $\boxed{6}$ surrounding the calorimeter produces a magnetic field of 1.2 T. The effect of the magnetic field on the beams is compensated by small solenoid $\boxed{7}$. Magnet yoke $\boxed{10}$ is made of iron stabs interleaved with streamer tube detectors for measuring hadronic energy escaping the main calorimeters. Muons are identified and measured by muon chambers $\boxed{9}$ inside and outside the iron. In the forward region muons are traced using forward muon spectrometer $\boxed{11}$ which consists of drift chamber planes mounted on either side of a toroidal magnet.

A detailed description of the H1 detector and its performance can be found in [22].

---

[7] The detectors in the backward region were upgraded in 1995 by replacement of the lead/scintillator tile calorimeter and a proportional chamber.

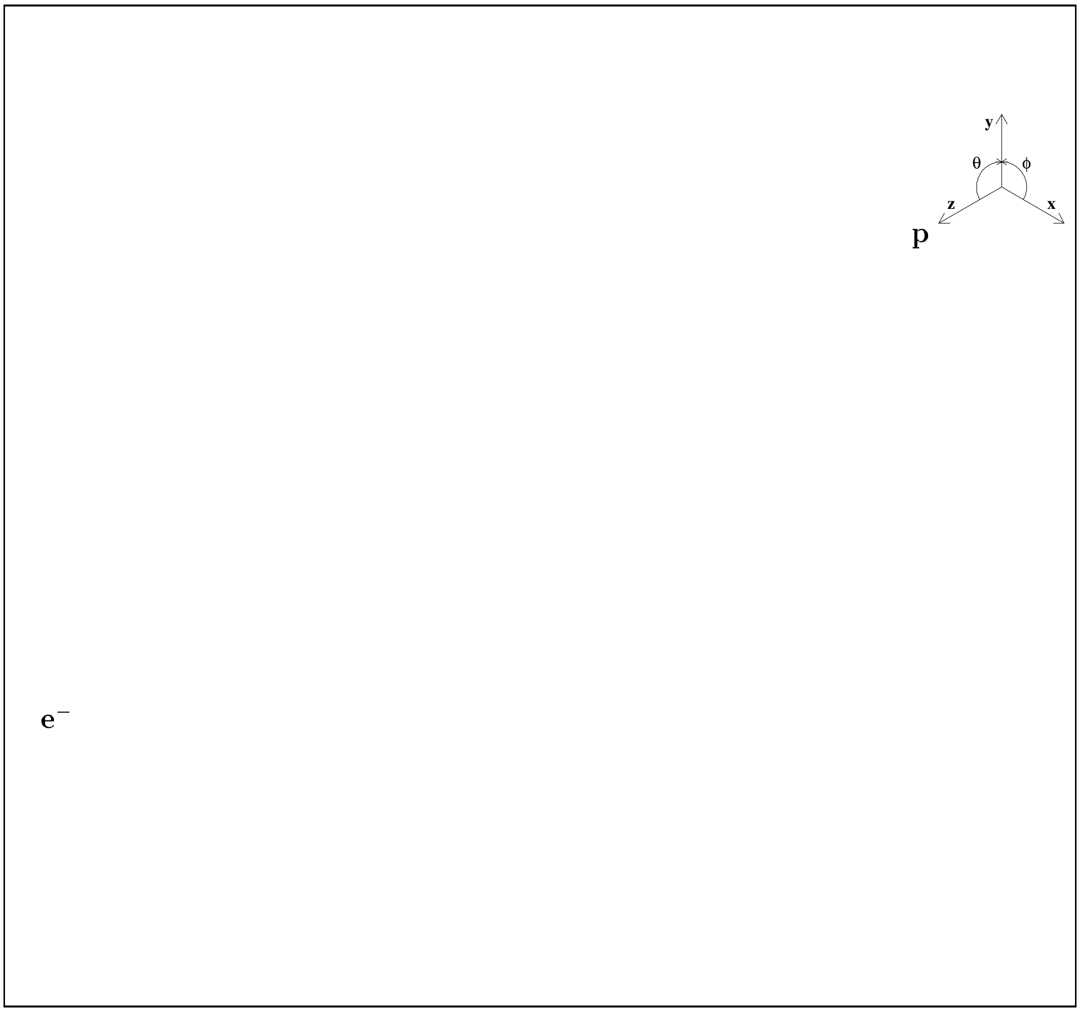

1 Beam pipe and beam magnets
2 Central tracking device
3 Forward tracking device
4 Electromagnetic LAr calorimeter
5 Hadronic LAr calorimeter
6 Superconducting coil (1.15 T)
7 Compensating magnet
8 Helium supply for 7
9 Muon chambers
10 Instrumented iron yoke
11 Forward muon toroid
12 Backw. electromagn. calorimeter (BEMC)
13 PLUG calorimeter
14 Concrete shielding
15 Liquid argon cryostat

Figure 5.1: *Schematic view of the H1 detector. Proton beam enters the H1 detector from the right and electrons from the left.*

Analysis of forward jets in deep inelastic scattering relies essentially on the liquid argon calorimeter (LAr), where the forward jets are measured, and the backward electromagnetic calorimeter (BEMC) which–with the help of BPC–provides parameters of the scattered electron. These parts of the H1 detector will be described in more detail.

5.2.1 Liquid Argon Calorimeter (LAr)

The H1 detector was designed to provide clear identification and precise measurement of electrons, muons and penetrating neutral particles together with very good performance in the measurement of jets with high particle densities. These requirements were best met by the calorimeter placed inside a large coil to minimize both the amount of dead material in front of the electromagnetic calorimeter and the overall size and weight of the calorimeter.

Liquid argon technique was chosen for the H1 calorimeter since it provides good stability, ease of calibration, fine granularity and homogeneity of response.

The LAr extends over the polar angular range of $4° < \Theta < 153°$ with full azimuthal coverage. Segmentation along the beam axis is done in eight self–supporting "wheels" as shown in Fig.5.2. Each of the six barrel wheels is segmented in ϕ into eight identical stacks or octants.

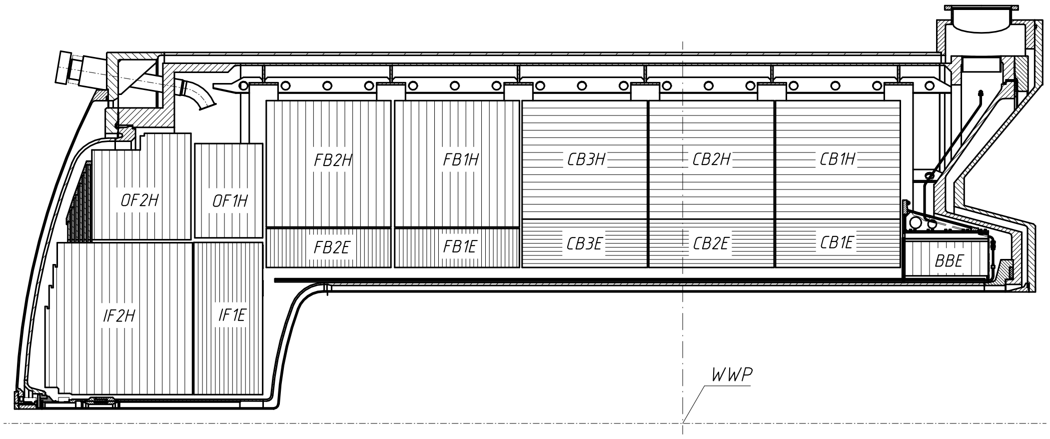

Figure 5.2: *Longitudinal view of the upper part of LAr calorimeter. WWP indicates the nominal interaction point.*

Longitudinally the calorimeter is subdivided into an electromagnetic section with lead plates, and a hadronic section with stainless–steel plates as absorbers. All plates are submerged in 70 m^3 of liquid argon, cooled to a temperature of $-183°$ Celsius. Orientation of the absorber plates is such that particles are incident on the calorimeter with angles not smaller than 45°. Both electromagnetic and hadronic sections are finely segmented in transverse and longitudinal directions with about 44 000 cells in total. Total depth of the calorimeter varies between 4.5 (in the central part) and 8 (in the forward part) interaction lengths. The calorimeter was optimized, using test bins, for a precise measurement and identification of electrons and hadrons. Energy resolution σ/E for electrons is $(12\%/\sqrt{E}[GeV]) \oplus 1\%$ ($\oplus$ means quadratic addition), and $(50\%/\sqrt{E}) \oplus 2\%$ for charged pions. Hadronic energy measurement is performed by applying a weighting technique in order to account for the non-compensating nature of the calorimeter. The absolute scale of hadronic energy is presently known to be 4% , as determined from studies of transverse momentum balance in DIS events.

5.2.2 Backward Electromagnetic Calorimeter (BEMC)

The Backward Electromagnetic Calorimeter covers polar angles from 155° to 176°.[8] Its primary task is to measure energies and directions of electrons scattered under small angles in deep inelastic processes. It also contributes to the measurement of hadrons emerging in photoproduction.

The BEMC is made of 88 lead–scintillator stacks aligned parallel to the beam pipe. Transverse structure can be seen in Fig.5.3. 56 stacks have a quadratic cross–section with a size of 16×16 cm^2. The remaining ones are of trapezoidal and triangular shapes in order to provide approximation to the circular shape of the support barrel. Depth of the stacks is 22 radiation lengths, which amounts to one interaction length. The scintillating light is read out transversely via wavelength shifters (WLS) covering full length of BEMC stacks. The four photodiodes which detect the wavelength shifted light from each of the scintillator stacks, provide a 1.5 cm spatial resolution of the lateral shower position.

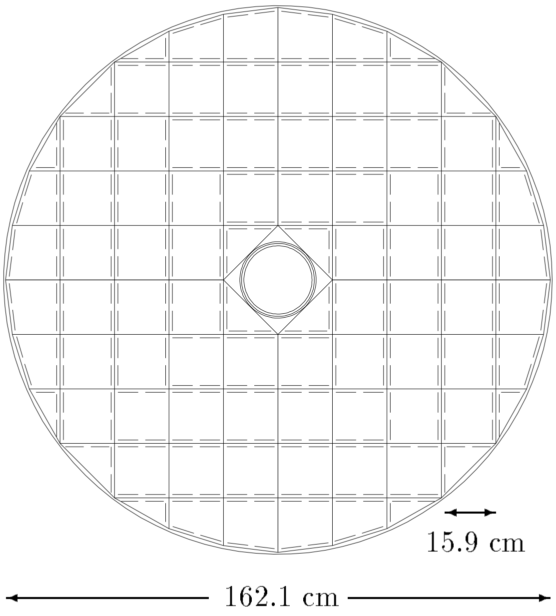

Figure 5.3: *Transverse view of the BEMC barrel. Positions of all WLS in the BEMC are marked.*

Space points for charged particles entering the BEMC are provided by a four–layer proportional multiwire chamber (BPC). These points are used to identify electrons (for $Q^2 < 120$ GeV) and to measure their polar angles. The polar angle acceptance of BPC

---

[8] The BEMC was replaced with a fibre backward calorimeter in 1995.

falls between 155.5° and 174.5°. Spatial resolution for reconstructed BPC hits is about 1.5 mm in the xy plane.

5.2.3 Luminosity measurement

Luminosity L is defined by the formula:

$$N = L\sigma \tag{5.1}$$

where N is the number of events coming from the process of cross–section σ .
Luminosity is determined from the rate of Bethe–Heitler process $ep \rightarrow ep\gamma$ because this process has a large and precisely calculable cross–section.

The luminosity monitor detects scattered electrons and outgoing photons in coincidence. Therefore, it contains two arms: the electron tagger (ET) and the photon tagger (PT). Since the angular distributions for both electrons and photons are strongly peaked in the direction of the incident electron beam, the detectors should be placed close to the beam line and very far from the interaction point (IP) in order to cover these small angles. The layout of the luminosity system is shown in Fig.5.4.

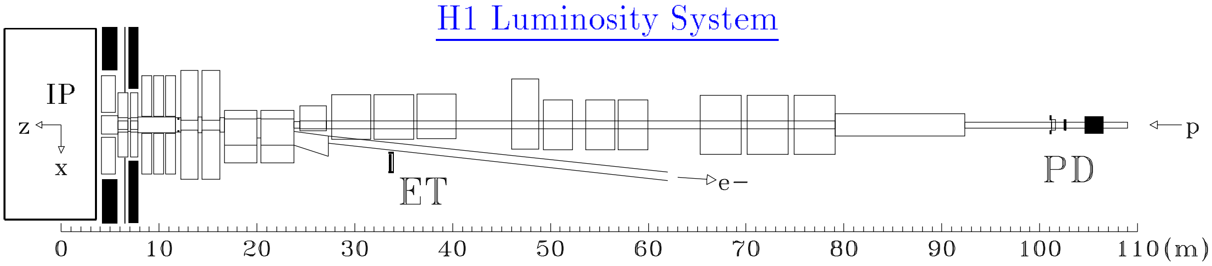

Figure 5.4: *General view of the luminosity system.*

Since the scattered electrons have energies smaller than the primary electron beam, they are deflected from the nominal orbit by the magnetic field. They leave the vacuum pipe through the exit window located at $z = -27.3\ m$ and hit the ET at $z = -33.4\ m$. Bremsstrahlung photons are not deflected in the magnetic field of the accelerator and they pass the photon exit window at $z = -92.3\ m$, where the proton beam pipe bends sideward, and hit the PT at $z = -102.9\ m$. The PT is protected from the synchrotron flux and the proton halo.

Total accuracy of the luminosity measurement, in the H1 experiment in 1994, was 1.5% .

Total integrated luminosity for 1994, as delivered by HERA and as used for the analysis, are shown in Fig.5.5.

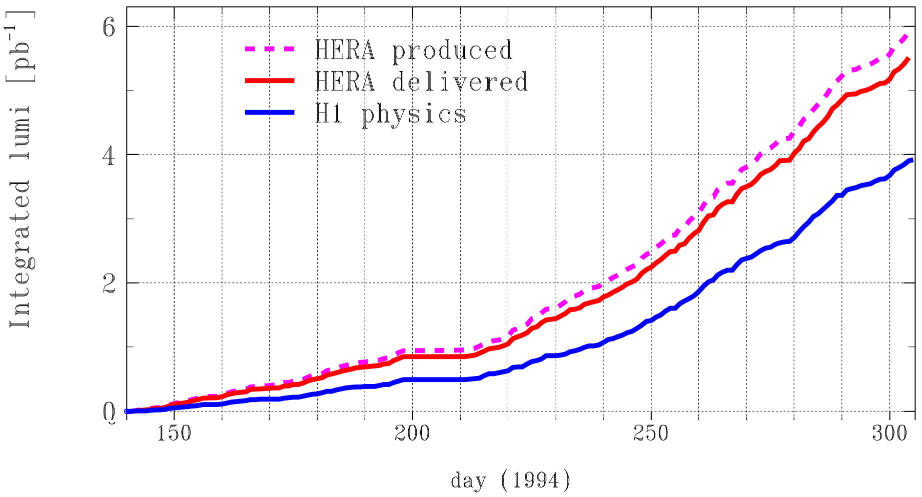

Figure 5.5: *Luminosity as produced (delivered) by HERA and as accumulated by H1 experiment in 1994 running period.*

5.2.4 Trigger

The purpose of the trigger system is to select interesting ep collision events and to reject background events. In order to deal with low cross–sections in ep physics, large proton and electron accelerator beam currents are required, which is only possible by running in a multibunch mode. That makes the task of separating interesting physics events from the background more difficult.

Three basic types of background the trigger has to handle are: synchrotron radiation from the electron beam, proton–gas interaction in the beam pipe and stray protons which produce particle showers by hitting the beam tube, and apertures around the accelerator. The H1 trigger decision is made in four steps called trigger levels. In 1994 second– and third–level triggers were not yet in use.

First–level trigger (L1).
In order not to lose luminosity delivered by HERA, first–level trigger has to be dead–time free. This goal is achieved by using the so–called front–end pipelines which keep detector information stored while first–level trigger calculations take place.
L1 consists of nine different trigger systems, each based on the information from a certain subdetector.
The most efficient trigger systems are the vertex position oriented ones because the origin from the nominal vertex area of the ep interaction region is the only unique feature which distinguishes ep events from most of the background.

Primary selection of deep inelastic scattering events is made by the calorimetric triggers:

- The liquid argon calorimeter trigger is designed to calculate energy deposited in various parts of the calorimeter as well as the total energy and other global energy sums which can be weighted by position–dependent weighting factors (e.g. for the total transverse energy, a weight of $sin\Theta$ is used).
  Missing total transverse energy of the liquid argon signal is used to identify charged current deep inelastic events, while the requirement of some electromagnetic but no hadronic energy deposited in a given position of the liquid argon calorimeter, spots the scattered electron in the neutral current event.

- The BEMC single electron trigger is built to identify electrons from DIS processes scattered into BEMC angular acceptance region. The basic concept of this trigger is to provide cluster recognition and to place energy thresholds on the sum of all energy clusters in the BEMC.

L1 reduces interaction rate from 50–100 kHz to $\sim$ 50 Hz.

Fourth–level trigger (L4).
L4 is a software filter farm designed to make final background reduction before data are sent to the storage media at the DESY computer center. It works asynchronously with the rest of the trigger. Calculations are performed by the processor farm based on raw data of full events. To make their decisions, filtering algorithms use information on charged tracks, vertex and energy clusters.
The aim of the L4 is reducing data rate to $\sim$ 5 Hz.

6 Data selection

Data used for this analysis were collected in 1994 and correspond to integrated luminosity of 2.82 pb^{-1}. Only 0.38 pb^{-1} out of it comes from the e^-p scattering; the remaining major part was produced in e^+p.

Event selection criteria can be divided into the following categories:

- general conditions,
- event vertex requirement,
- electron identification and DIS selection,
- forward jet selection,
- background rejection.

The total sample of 1994 H1 data prepared for physics analysis contains about 10.5 million events. 97% of these events are rejected due to trigger, detector requirements, vertex cuts and DIS selection. The forward jet requirements and the background rejection cuts select the final sample used in this analysis. It contains 2000 events.

More details about the selection criteria will be given in the next subsections.

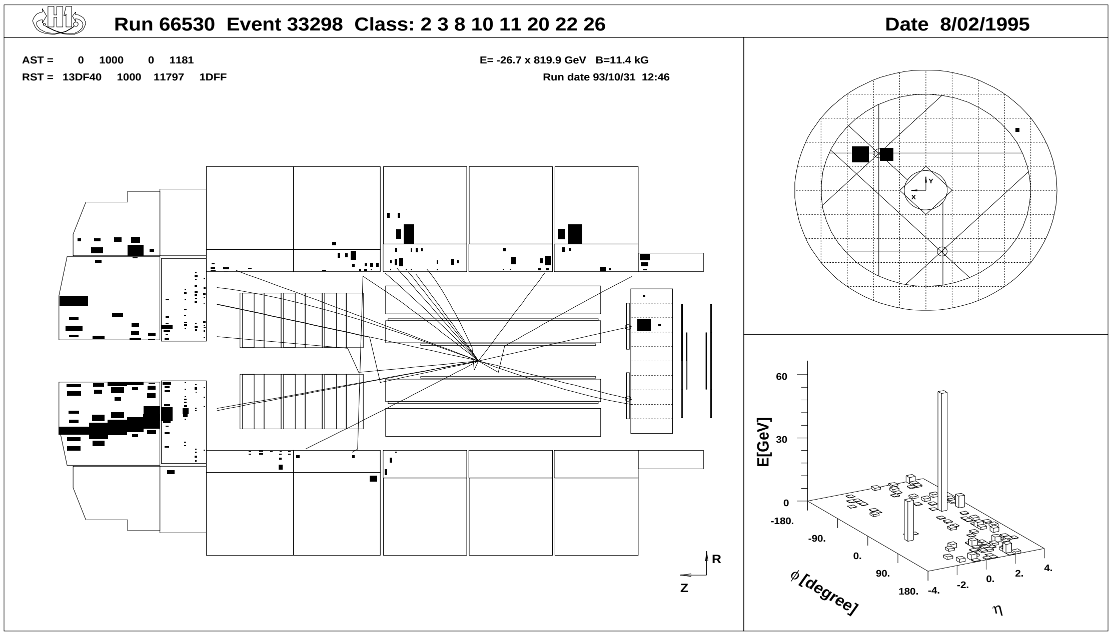

Figure 6.1: *A forward jet event in the H1 detector.*
Protons are coming from the right, electrons from the left. Scattered electron is detected in the BEMC at an angle of 166^o *and energy of 18.9 GeV. The forward jet is observed in the liquid argon calorimeter at an angle of* 11^o *and energy of 65 GeV. The upper right plot shows projection of BEMC clusters and BPC hits. The lower–right plot illustrates energy flow as a function of azimuthal angle* ϕ *and pseudorapidity* η*.*

A typical forward jet event (see Fig.6.1) is characterized by an energetic jet in the forward part of the calorimeter, an electron cluster in BEMC and some activity – originating from the struck quark – in the central part of the calorimeter. We want to stress that the forward jet we have been looking for in this measurement is different from the jet originating from the scattered quark – the so–called current jet.

6.1 General conditions

First, run conditions are checked. We accept events from runs of good or medium quality. For good quality runs, all major detector systems have to be operational. For medium quality runs, one major system or several minor systems may be out of operation.

We also require that all parts of the H1 detector needed for the forward jet analysis, i.e., CJC1, CJC2, BPC, BEMC, TOF and LAr operate properly.

Events are triggered by requiring a cluster of more than 4 GeV in the BEMC.

6.2 Event vertex requirements

The event vertex position is needed for precise determination of kinematics. It is defined by at least one well measured track in the CJC or in the forward tracker (FT) crossing the beam axis. The z position of the event vertex has to be $z = (5 \pm 35)\ cm$.

6.3 Electron identification

The scattered electron is defined as the most energetic BEMC cluster. Its centre of gravity is required to be at a radial distance smaller than 4 cm from a reconstructed BPC point. The lateral size of that cluster, calculated as energy–weighted radial distance of the cells from the cluster centre, has to be smaller than 4 cm.

The energy of the scattered electron is required to be larger than 11 GeV. In order to ensure high trigger efficiency and a small photoproduction background, the electron polar angle – Θ_e has to be below 173^o, and in order to make sure that the electron cluster is fully contained in the BEMC – Θ_e above 160^o is needed. Θ_e is defined with respect to the incident proton beam direction ($+z$ axis).

6.4 Event kinematics

Kinematical variables in HERA experiments can be reconstructed in different ways using measured quantities from the hadronic final state and from the scattered electron. In this analysis we have chosen the electron method. This method uses only the scattered electron energy E_e and angle Θ_e:

$$Q^2 = 2E_{eb}E_e(1 + \cos\Theta_e) \tag{6.1}$$

$$Y = 1 - (\frac{E_e}{2E_{eb}}(1 - \cos\Theta_e)\ , \tag{6.2}$$

where E_{eb} is the incident electron beam energy.
x_B is obtained from formula 2.1: $x_b = Q^2/ys$.

6.5 Forward jet selection

In further selection, DIS events at small x_B which have a forward jet, i.e. a jet emitted at polar angle $7^o < \Theta_{jet} < 20^o$ with respect to the proton beam direction, are chosen. The lower limit of Θ_{jet} should be high enough to avoid collecting the remnant jet and to ensure that the selected jet is almost completely contained in the calorimeter. The upper limit of Θ_{jet} keeps the forward jet in the forward part of the calorimeter, so it may not be faked by the current jet. The jet is parametrized by the longitudinal momentum x_{jet} and the transverse momentum squared p^2_{Tjet}. There, $0.5 < p^2_{Tjet}/Q^2 < 2$ is required, which, due to strong ordering, leaves little room for the DGLAP evolution. Simultaneously, phase space for the BFKL evolution is maximized by the condition $x_{jet} \gg x_B$, which in our analysis is achieved by cuts $0.0001 < x_B <0.004$ and $x_{jet} \approx E_{jet}/E_p > 0.035 \Leftrightarrow E_{jet} > 28.7$ GeV , where E_p is proton beam energy.

A cone algorithm is used to find jets. The idea of a cone algorithm is the following: all objects (partons, hadrons or calorimeter cells) are placed in the space of pseudorapidity, η, and azimuthal angle, ϕ, in the HERA frame of reference. Then a cone of radius $R = \sqrt{\Delta\eta^2 + \Delta\phi^2} = 1.0$ is moved in this space in order to find such a position where the net transverse momentum p_T of all objects inside the cone is the highest. If $p_T > 3.5$ GeV, these objects are defined as a jet, they are locked and the procedure starts again for all remaining cells. The four–momentum of a jet is defined as the sum of four–momenta of all objects the jet is built of. Knowing the jet four–momentum one can calculate the position (the azimuthal and polar angles) of the jet axis.

6.6 Background rejection

Measurement of the forward jet cross–section may be distorted by several groups of events which fulfill all selection cuts mentioned above but do not originate from the process under study. Two main sources of background may be distinguished: the background to DIS (beam–gas, beam–wall, photoproduction) and the DIS events containing a forward jet that does not originate from the "ladder" (QED radiation events and pile-up effect).

6.6.1 Non–ep background

For our sample the main sources of non-ep background are due to proton beam interactions with the residual gas and with the beam line elements upstream the H1 detector. This background is effectively removed by the vertex and electron requirements. The remaining background estimated from the study of pilot bunches represents less than 1% of the total number of selected events (based on studies for F_2 in H1 [5]).

6.6.2 Photoproduction background

Electron-proton collisions in which an almost real photon is exchanged are called photoproduction. The final state electron in these events is scattered through a very small angle, yielding $10^{-7} < Q^2 < 2\cdot 10^{-2}$ at the HERA experiments.

In the case of photoproduction background, the scattered electron escapes down the beam pipe and a fake electron is identified from energy deposits in the BEMC. This source of background is quite effectively rejected by the electron identification requirements, especially by the electron energy cut $E_e > 11$ GeV.

Further reduction of the photoproduction background is achieved by requiring $E - P_z = \sum_j (E_j - p_{z_j}) > 35$ GeV, where the sum extends over all calorimeter cells. Using energy and momentum conservation and the fact that $E - P_z$ is negligible in the forward beam pipe, one may see that the energy of any particle of energy E_x escaping through the backward beam pipe is given by:

$$E - P_z = 2(E_{eb} - E_x).$$

Thus, for DIS events the distribution of $E - P_z$ is peaked around $2E_{eb}$ and photoproduction events have $E - P_z$ smaller due to the loss of the scattered electron.

In order to estimate the remaining background, photoproduction events generated with PYTHIA5.7 [23] and RAYVDM2.0 [24] are used. Contamination of the photoproduction background in the final sample is below 4%. Most of it (>80%) has x_B below 0.0005 and no photoproduction event is found for $x_B > 0.001$. The background is subtracted statistically.

6.6.3 Pile–up effect

For the process under consideration, another possible source of background is an accidental overlap of a DIS event which produces an electron in BEMC, with beam–gas or beam–wall events which produce a high energy jet in the forward region. We studied this effect for the 1993 data and found it to be negligible (below 1%).

6.6.4 Radiative background

In order to ensure that the current jet – the jet coming from the struck quark – is in the central region (so it cannot fake the forward jet), the condition $y_B > 0.1$ was imposed. However, in the case of the QED initial state radiation (ISR), i.e. when an energetic photon is radiated off the incoming electron, the calculation of electron and kinematic variables is no longer correct. This background is partly removed by cuts mentioned above, e.g. $\sum_j (E_j - p_{z_j}) \approx 2E_{eb} - 2E_\gamma > 35$ GeV, where E_γ is energy of the photon emitted off the incoming electron. To study the remaining ISR background MC events produced with DJANGO generator[9] are used. In order to make sure that the current jet is not emitted in the forward direction we require some activity in the central calorimeter. For this purpose, variable Θ_{max} is introduced. By definition, $\Theta_{max} \overset{\text{def}}{=} \max\{\Theta_i\}$, where i runs over all clusters which have energies $E_i > 0.3$ GeV and are fully contained in the hadronic calorimeter (i.e. $\Theta_i < 160^o$). In Fig.6.2 distribution of Θ_{max} for DJANGO events surviving all selection cuts is shown. The shaded part corresponds to those events where photon of energy $E_\gamma > 3$ GeV is radiated off the incoming electron.

The requirement $\Theta_{max} > 45^o$ reduces the QED ISR background by 55% and losses 5% of real forward jet events.

When data correction to the hadron level is done with radiative MC (DJANGO), we use true variables at the generator level, i.e. those which take into account the fact of the

---

[9] As mentioned in Section 4, QED radiation is implemented in DJANGO.

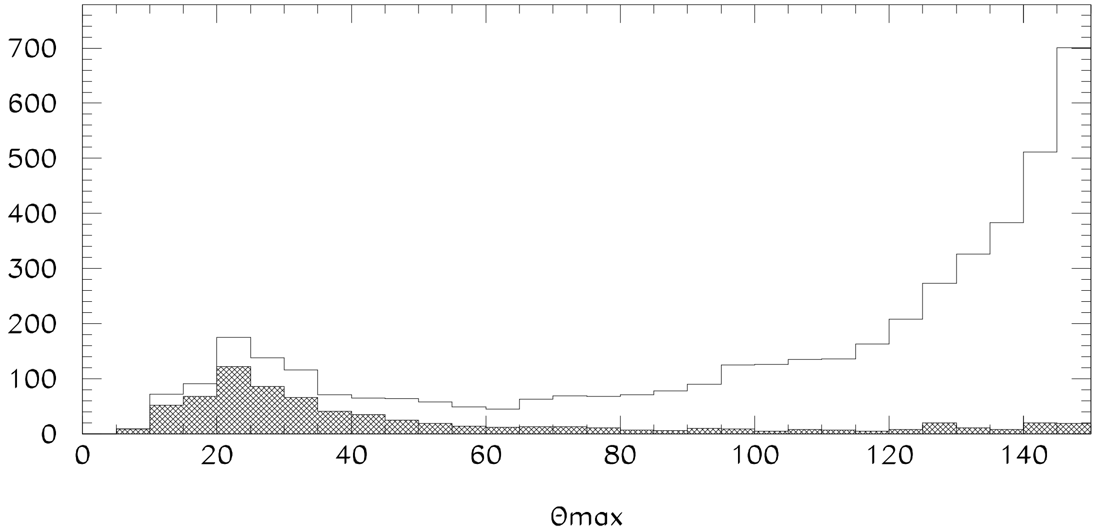

Figure 6.2: Θ_{max} *distribution for DJANGO events fulfilling all selection conditions. Shaded part shows ISR contribution.*

photon emission. This enables us to correct for inefficiency of the Θ_{max} cut, i.e. to find back the genuine forward jet events lost due to the Θ_{max} cut, and to reject the remaining radiative background.

When we correct the data with a non–radiative MC (LEPTO6.5), we apply the Θ_{max} cut both to the data to remove radiation and to the MC detector level events in order to be able to recover – in unfolding – the real forward jet events rejected by the Θ_{max} cut. In this case, the remaining radiation is, estimated from DJANGO and subtracted statistically bin by bin.

6.7 Cuts summary

Cuts defining the phase space for the forward jet analysis are collected in Table 6.1.

$E_e > 11$ GeV
$160^o < \Theta_e < 173^o$

$0.0001 < x_B < 0.004$
$y_B > 0.1$

$p_{T_{jet}} > 3.5$ GeV
$E_{jet} > 28.7$ GeV $\Leftrightarrow x_{jet} > 0.035$
$7^o < \Theta_{jet} < 20^o$
$0.5 < p^2_{T_{jet}}/Q^2 < 2.$

Table 6.1: *Standard cuts for forward jet analysis.*

Sample purity cuts, e.g. Θ_{max}, are applied to the data only, therefore they are not included in the table.

Kinematical area with limits introduced by the cuts described above is shown in Fig.6.3. Dots indicate population of the forward jet events.

6.8 Monte Carlo models used in the analysis

In this analysis we use events generated by two Monte Carlo models:

- DJANGO 6 – contains HERACLES 4.4 and ARIADNE 4.05 models and uses JETSET 7.404 for hadronization,
  matrix elements are not implemented in this MC, and QCD cascades are simulated using the CDM model implemented in ARIADNE. Therefore, in this thesis the Monte Carlo model will always be referred to as a CDM model.

- LEPTO6.5 – incorporates the MEPS (Matrix Elements + Parton Shower) model, so we will refer to it as a MEPS model. It also uses JETSET7.404 for hadronization.

DJANGO6 Monte Carlo events were generated for the purpose of this analysis. The generator file contains 900 000 events – corresponding to total luminosity of 7 pb^{-1}. These events were preselected at hadron level in the following way:
electron energy $E_e > 8$ GeV,
polar angle of electron $159° < \theta_e < 174°$,
$y > 0.05$,
jet energy $E_{jet} > 12$ GeV,
jet transverse momentum $p_{Tjet} > 2$ GeV,

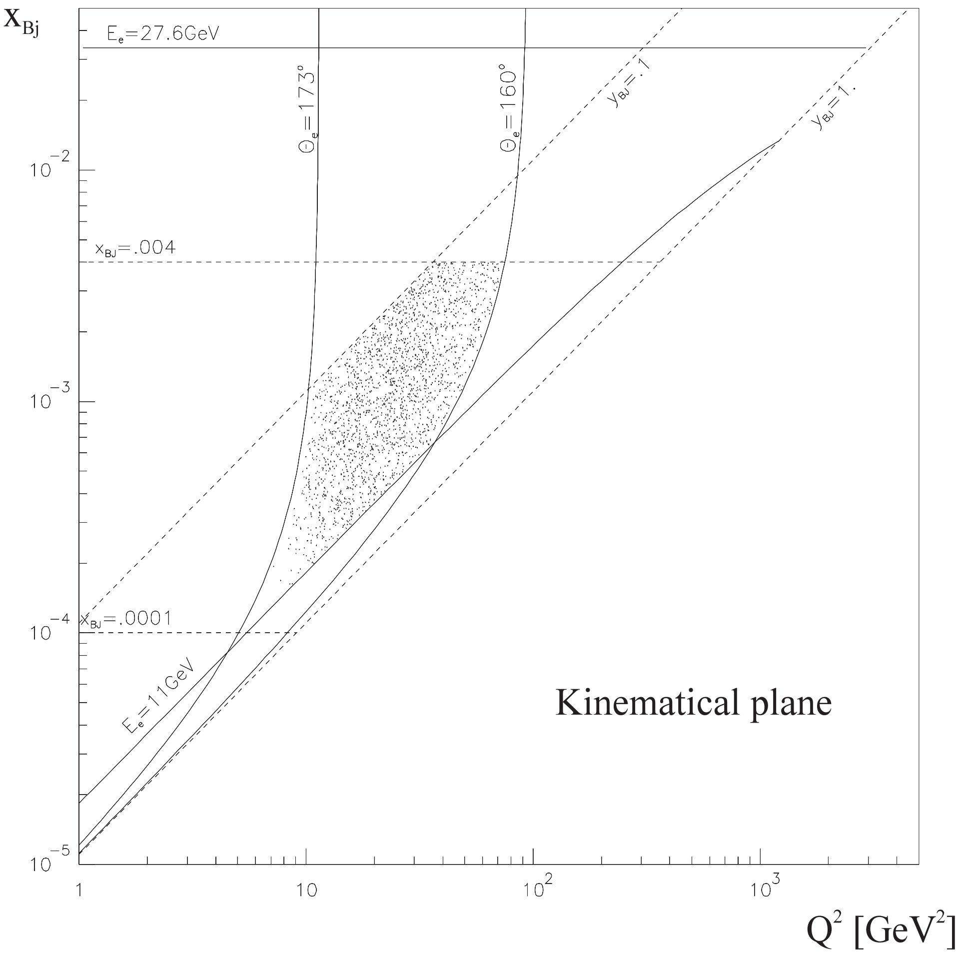

Figure 6.3: *Kinematical area available for forward jet measurement. Dots illustrate data distribution.*

and jet polar angle $3° < \theta_{jet} < 30°$.
After preselection, less than 250 000 events were left and only these events were fed into the H1 detector simulation program and processed through the same reconstruction and analysis chain as the data.
Unpreselected Monte Carlo files are used to check to what extent the sample is biased by preselection. We find that 2% of the events which fulfill all cuts at detector level are rejected by preselection.

Events generated with LEPTO6.5 were not preselected. We use files containing about 600 000 events, corresponding to total luminosity of 3.8 pb^{-1}.

6.9 Comparison of data and Monte Carlo distributions for electron and kinematic variables

In this analysis we use Monte Carlo events to unfold data from all distortions caused by detector effects and reconstruction methods. Monte Carlo models are also used for final presentation of our results. We compare the forward jet cross–section with predictions given by different Monte Carlos. Therefore, it is quite essential that before we start our analysis we make sure that the Monte Carlo models we use describe basic distributions of the DIS data. For this purpose we select data and Monte Carlo events only with the DIS cuts. In Fig.6.4 basic distributions of electron (energy, polar angle – Θ, azimuthal angle – ϕ) and kinematical (x_B, Q^2 and y) variables are shown. The data are denoted with + where the vertical line corresponds to the statistical error, while the CDM and MEPS distributions are plotted with dashed and dotted lines, respectively.

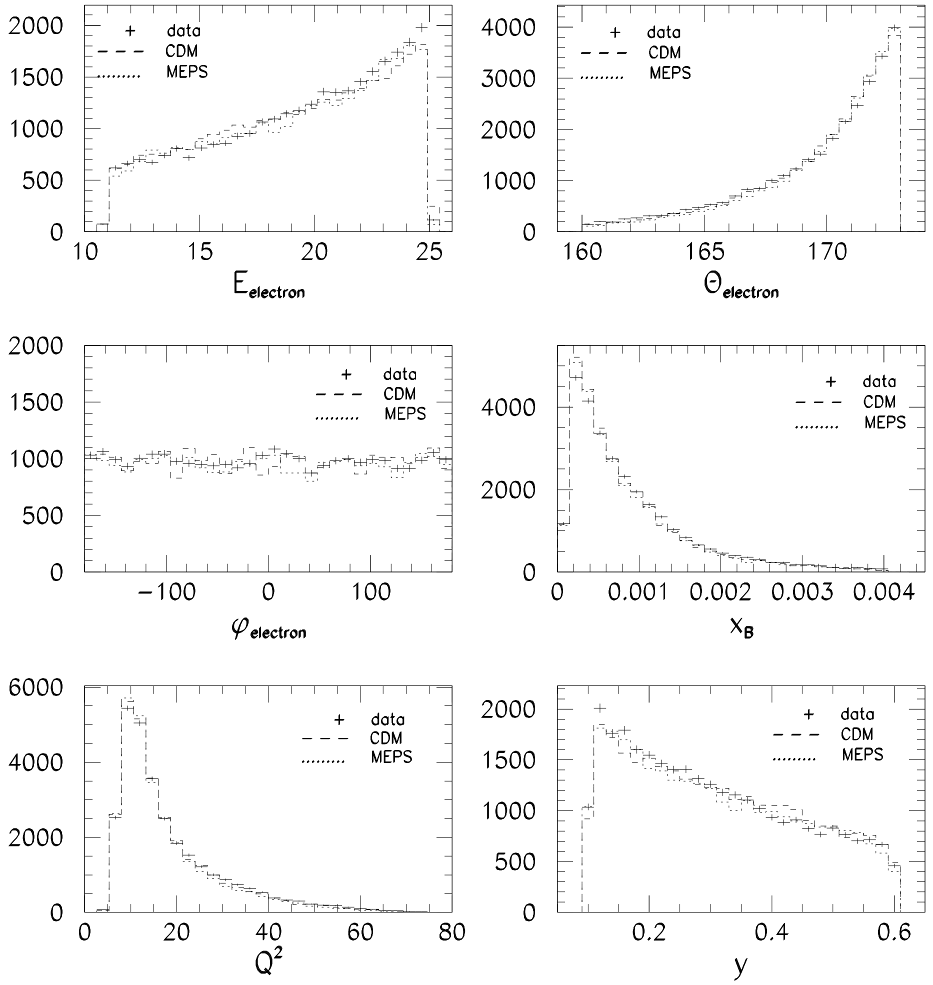

Figure 6.4: *Comparison of electron and kinematical variable distributions for the DIS data with CDM and MEPS Monte Carlo models.*

One may see that the MC models are able to reproduce the data quite well.

7 Jet studies

In order to relate the hadronic final state measured in the calorimeter to hard partonic processes, a jet finding algorithm is necessary. As already mentioned, in this analysis a cone algorithm – defining jets by transverse momentum deposited in a cone of radius R=1 in the pseudorapidity–azimuthal angle plane – is used.

In this section results of the studies of jet profiles and shapes will be presented.

7.1 Jet profiles

Flow of transverse energy E_T, averaged over all selected events, as a function of $\Delta\phi$, integrated over $|\Delta\eta| < 1$, is shown in Fig.7.1(a.), and as a function of $\Delta\eta$, integrated over $|\Delta\phi| < 1$ – in Fig.7.1(b.). $\Delta\eta$ and $\Delta\phi$ are distances of calorimeter cells from the reconstructed jet axis in pseudorapidity η and azimuthal angle ϕ. Data distributions are plotted with full circles, and statistical errors are depicted as well. Predictions of the CDM and MEPS Monte Carlo models are shown with dashed and dotted lines, respectively.

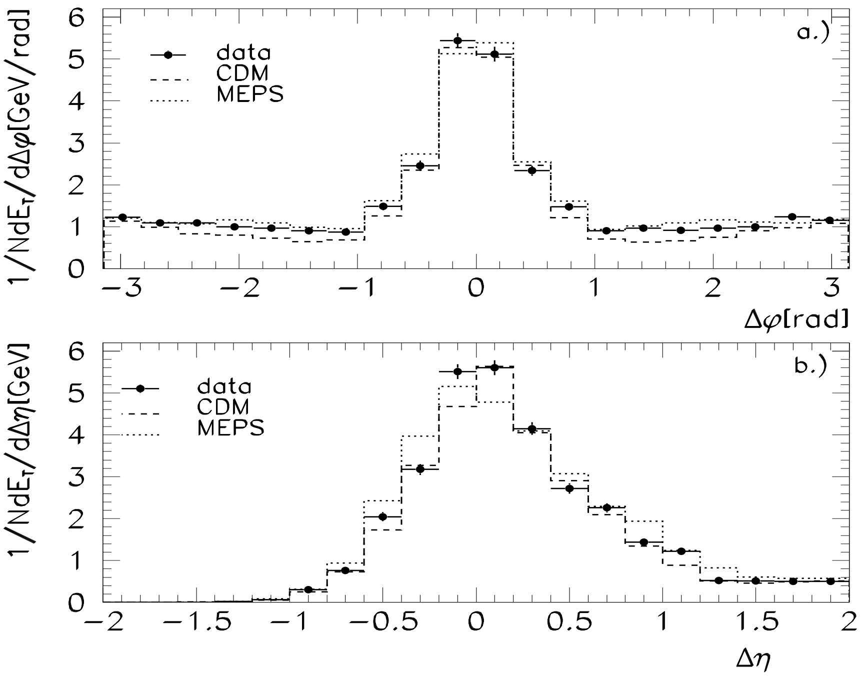

Figure 7.1: *Transverse energy flow around the forward jet axis, averaged over all selected events, integrated over* $|\Delta\eta| < 1$*, as a function of* $\Delta\phi$ *- (a.) and integrated over* $|\Delta\phi| < 1$*, as a function of* $\Delta\eta$ *- (b.).*

Data points are plotted with full circles, CDM and MEPS Monte Carlo models are plotted with dashed and dotted lines, respectively.

Distinct jet profiles are observed. Simulations of the QCD models (MEPS and CDM) reproduce gross features (i.e. shape and height) of the observed $\Delta\eta$ and $\Delta\phi$ jet profiles. Some asymmetry due to the forward detector acceptance may be noticed in Fig.7.1(b.)

More precise studies of the jet profiles show that jets – particularly those emitted at low angles – suffer from proximity of the beam–pipe and the proton remnant.

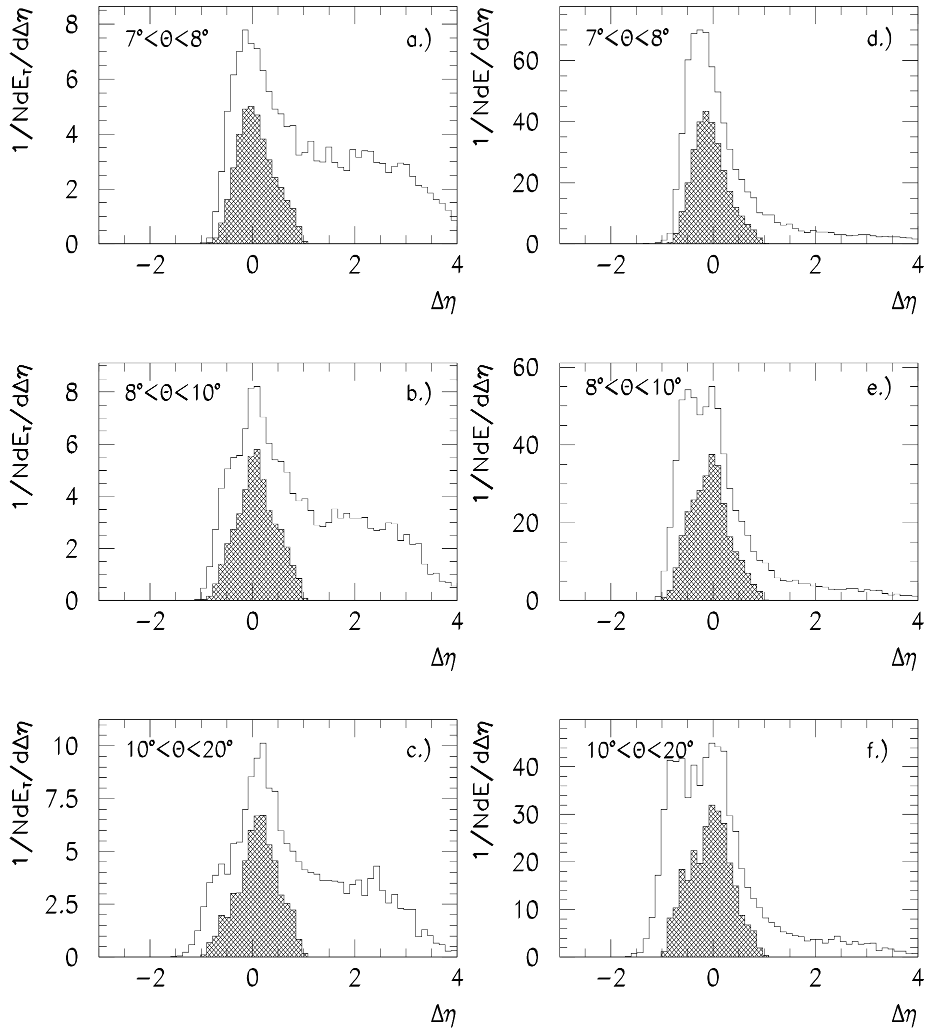

Figure 7.2: *Transverse energy (a.-c.) and energy (d.-f.) flows around the forward jet axis for different* Θ_{jet} *bins for jets at detector level. Shaded parts show contributions integrated over* $|\Delta\phi| < 1$*, while for the empty histogram integration area covers the full range of* $\Delta\phi$*.*

Fig.7.2(a.-c.) shows transverse energy flow around the jet axis as a function of $\Delta\eta$ for different Θ_{jet} ranges. Shaded part is integrated over $|\Delta\phi| < 1$ and the empty one is integrated over the full range of $\Delta\phi$, i.e., $|\Delta\phi| < \pi$.

It may be seen from asymmetry in the jet profiles that for lower Θ_{jet} jets are quite close to the edge of the calorimeter, so a small part of the jet is lost in the beam pipe. This may cause e.g. underestimation of the jet energy.

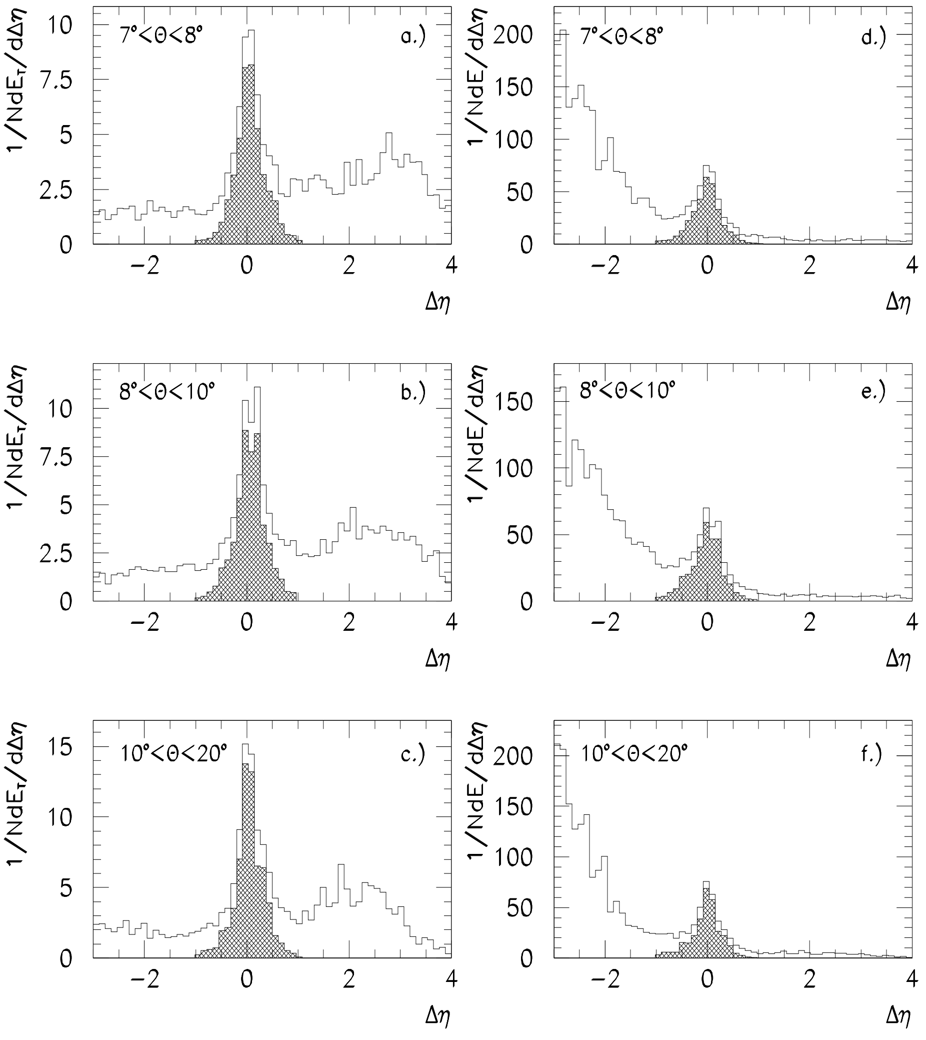

Figure 7.3: *Transverse energy (a. - c.) and energy (d. - e.) flows around the forward jet axis for different* Θ_{jet} *bins for hadron level jets. Shaded parts show contributions integrated over* $|\Delta\phi| < 1$*, for the empty histogram integration area covers the full range of* $\Delta\phi$*.*

On the other hand, jet measurement at low angles may be disturbed by the presence of some extra energy coming from the proton remnant jet. This may lead to overestimation of jet energy. In Fig.7.2(a.-c.) no two–jet structure or significant contributions from the proton remnant jet are seen. However, this changes when – instead of transverse energy flow – we plot energy flow around the jet axis – Fig.7.2(d.-f.). In Fig.7.2(e.-f.) two-peak structure may be noticed: one peak originates from the forward jet, but the other one (the one closer to the beam–pipe) may be due to the remnant jet. For the lowest angles (see Fig.7.2(d.) both these structures are united. This may result in some deformities in the measurement of jet parameters.

Fortunately, at hadron level jet profiles are distorted neither by the remnant jet nor by the beam–pipe. Fig.7.3 shows plots similar to those from Fig.7.2 but for jets at hadron level. One may notice that jet profiles are now quite symmetrical and remnant contributions are well separated from the forward jets. This enables us to use the unfolding procedure to correct for deformities caused by the beam-pipe and remnant jet effects.

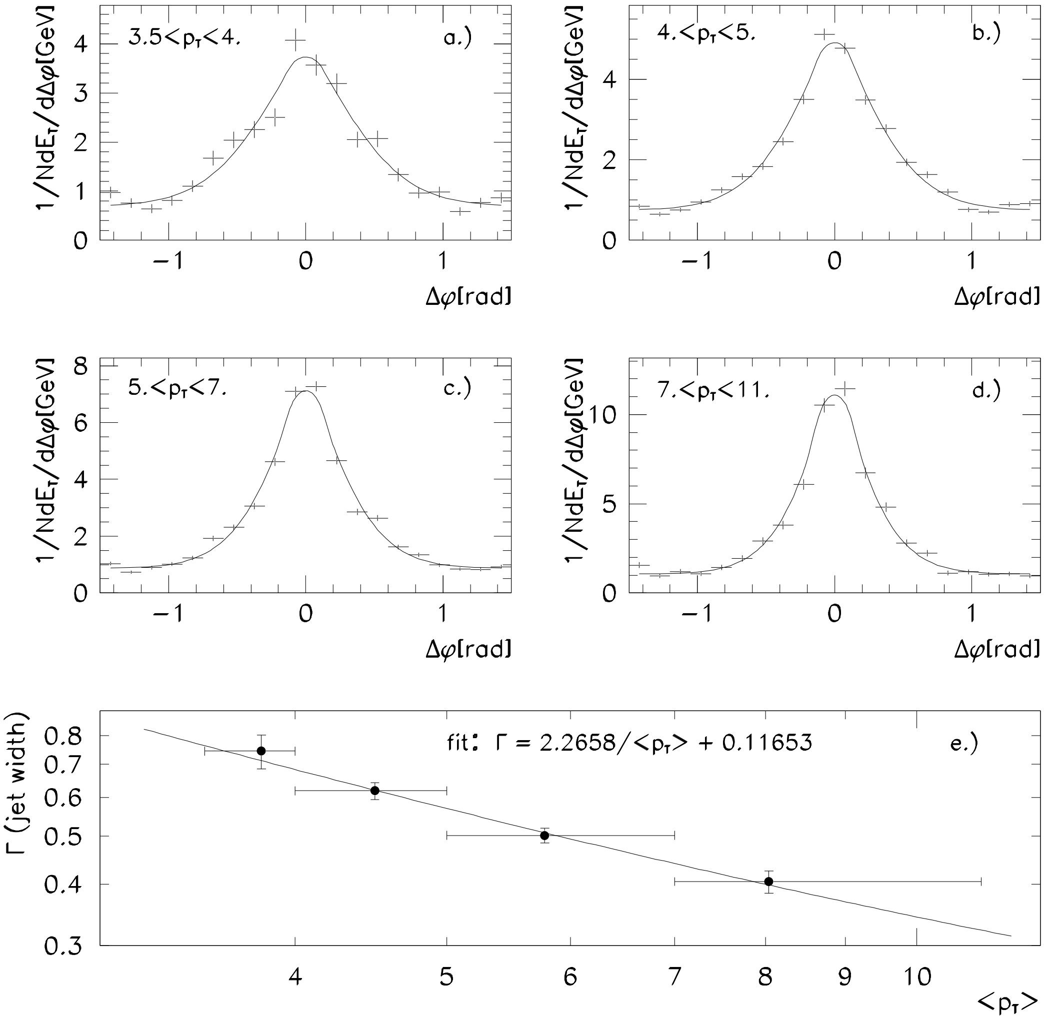

Figure 7.4: *(a.–d.): ϕ jet profiles for different p_T intervals.*
(e.): Γ – $\langle p_T \rangle$ dependence with the fit motivated by QCD.

7.2 Jet widths

QCD predicts [25] that widths of the jet profiles should scale like $1/p_T$, where p_T is the transverse momentum of the jet.

In order to check if the jets selected in this analysis agree with this prediction, the selected sample is divided into four groups according to the forward jet transverse momentum:

a.) 3.5 GeV $< p_T <$ 4.0 GeV

b.) 4.0 GeV $< p_T <$ 5.0 GeV
c.) 5.0 GeV $< p_T <$ 7.0 GeV
d.) 7.0 GeV $< p_T <$ 11.0 GeV

Fig.7.4(a.-d.) shows $\Delta\phi$ jet profiles for various p_T subsamples. The profiles are fitted using the following parametrized form [26]:

$$f(\Delta\phi) = A\exp(-(\sqrt{|\Delta\phi|} + b)^4 + b^4) + P \ . \tag{7.1}$$

Full width at half maximum above pedestal is:

$$\Gamma = 2((\ln 2 + b^4)^{1/4} - b)^2 \tag{7.2}$$

In Fig.7.4(e.), Γ dependence on p_T is illustrated. The error on Γ determination is estimated from the fit range. The position of a point in the p_T bin corresponds to the mean value of the p_T distribution in this bin. The QCD motivated function [25]: $\Gamma \sim 1/\langle p_T \rangle$ was fitted. One can easily see that jet widths – even for jets with the lowest $\langle p_T \rangle$ (the first bin) – really scale like $1/\langle p_T \rangle$.

8 Data correction – Bayes unfolding procedure

Distributions measured in an experiment always differ from the true ones due to physics (e.g. QED ISR, hadronization) and detector effects. Original distributions may be distorted by trigger, selection cuts, reconstruction methods, detector acceptance or resolution.

The role of the experimentalist is to unfold observed distributions from all these deformations in order to extract the true distribution. This requires a satisfactory knowledge of an overall effect of the distortions on the true physical quantity.

There exist many different unfolding techniques. The simplest and quite often used approach is *bin-to-bin* correction. It is based on a *generalized efficiency* (it can be larger than unity) evaluated with the Monte Carlo as the ratio between the number of events falling in a certain bin of the reconstructed variable and the number of events in the same bin of the true variable. *Generalized efficiency* is then used to estimate the number of true events from the number of events observed in that bin. This approximation cannot take into account large migrations between bins and neglects unavoidable correlations between adjacent bins.

A method that has been developed to solve the problem of migrations and correlations is based on inversion of transformation matrix. Transformation matrix connects the number of events generated in one bin with numbers observed in other bins. Disadvantages of this method are: problems with matrix inversion and inability to handle large statistical fluctuations that may lead to negative numbers of unfolded events. These problems are overcome in the method called "regularized unfolding" [27] which becomes more and more popular in unfolding one-dimensional distributions.

Bayes' theorem also offers a way to unfold experimental distributions. This unfolding method does not require matrix inversion; it may deal with multidimensional problems and can take into account any kind of smearing and migrations from the true values to the observed ones. The method was proposed by G. D'Agostini in [28]; he also implemented it into a Fortran code.

8.1 Multidimensional unfolding method based on Bayes' theorem

In case of n_C independent causes that may produce effects E_j, Bayes' theorem states: "the probability $P(C_i/E_j)$ that the effect E_j is due to the i-th cause is proportional to the initial probability of the cause $P(C_i)$ times the conditional probability of the cause to produce the effect $P(E_j/C_i)$".

$$P(C_i/E_j) = \frac{P(E_j/C_i) \cdot P(C_i)}{\sum_{l=1}^{n_C} P(E_j/C_l) \cdot P(C_l)} \tag{8.1}$$

Let us note that:

- $P(E_j/C_i)$ called the transformation matrix must be estimated, e.g. with Monte Carlo methods, from the knowledge of overall effects of distortions in the initial distributions.

- $\sum_{i=1}^{n_C} P(C_i/E_j) = 1$, i.e. each effect must result from one or more causes under examination.
- $0 \leq \epsilon_i \equiv \sum_{j=1}^{n_E} P(E_j/C_i) \leq 1$, i.e. there is no need for each cause to produce one of the effects. ϵ is efficiency of detecting cause C_i in any of the possible effects.

A weak point of the Bayes approach is the need to know the initial distribution. This disadvantage may be overcome by the iterative procedure, since the Bayes formula has the power to increase our knowledge of $P(C_i)$ with the number of observations increasing.

After N_{obs} experimental observations one obtains a distribution of frequencies $n(E) \equiv \{n(E_1), n(E_2), ..., n(E_{obs})\}$. The expected number of events to be assigned to each of the causes ($\hat{n}(C) \equiv \{\hat{n}(C_1), \hat{n}(C_2), ..., \hat{n}(C_{obs})\}$) can be estimated taking into account efficiency ϵ:

$$\hat{n}(C_i) = \frac{1}{\epsilon_i} \sum_{j=1}^{n_E} n(E_j) \cdot P(C_i/E_j) \qquad \epsilon_i \neq 0 \ , \tag{8.2}$$

where $n(E)$ is the measured distribution observed in experiment and $\hat{n}(C)$ is the true distribution we want to find.
Matrix $P(C_i/E_j)$ called *smearing matrix* acts as inverted matrix in the matrix inversion method, but is obtained in a much easier way (no matrix inversion operation is needed).

From the unfolded events the true total number of events, final probabilities of the causes and overall efficiency can be estimated:

$$\hat{N}_{true} = \sum_{i=1}^{n_c} \hat{n}(C_i) \tag{8.3}$$

$$\hat{P}(C_i) \equiv P(C_i/n(E)) = \frac{\hat{n}(C_i)}{\hat{N}_{true}} \tag{8.4}$$

$$\hat{\epsilon} = \frac{N_{obs}}{\hat{N}_{true}} \tag{8.5}$$

Initial distribution $P_0(C_i)$ may differ from final distribution $\hat{P}(C_i)$ if $P_0(C_i)$ does not agree with the true one. The $\hat{P}(C_i)$ is between $P_0(C_i)$ and the true distribution. This suggests an iterative procedure that may be performed in the following steps:

1. selecting initial distribution $P_0(C_i)$ from our best information on the process under study, in case of complete ignorance setting $P_0(C_i)$ to a uniform distribution;
2. calculating $\hat{n}(C_i)$ and $\hat{P}(C_i)$;
3. performing χ^2 comparison between $\hat{n}(C_i)$ and $n_0(C_i)$;
4. replacing $P_0(C_i)$ with $\hat{P}(C_i)$, and $n_0(C)$ with $\hat{n}(C_i)$ and starting again; if χ^2 is "small enough" after the second iteration – iteration stops, otherwise – next iteration starts (return to step 2).

8.2 Unfolding of the forward jet cross-section

As explained in Section 3.1, the forward jet process we are interested in has to fulfill a set of theoretical conditions. For experimental purposes these conditions are translated into several cuts which – while taking into account the experimental conditions – explain how high is "high enough" or how low is "very low" in our measurement.

Since distribution of each physical quantity may be distorted during measurement, we need to find out true distributions of all variables crucial for the process under study. This leads to multidimensional unfolding. Effects E_j are observations of an event in a bin of measured quantities $(x_B, p^2_{Tjet}/Q^2, \Theta_{jet}, E_{jet})_{meas}$ and causes C_i are all possible bins of true values $(x_B, p^2_{Tjet}/Q^2, \Theta_{jet}, E_{jet})_{true}$. As the initial distribution $P_0(C_i)$, the Monte Carlo distribution at the hadron level is used.

8.2.1 Bin selection, correlations between hadron and detector levels – purity and efficiency

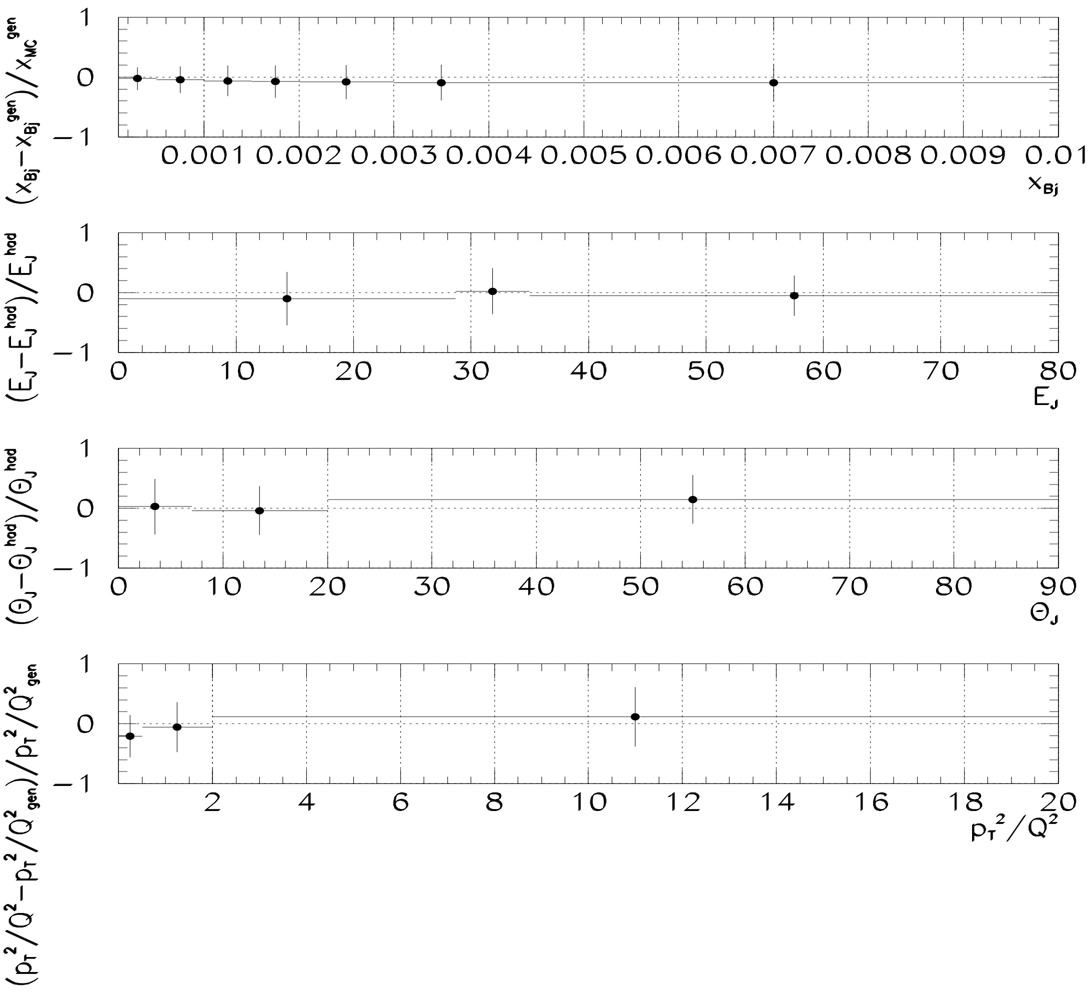

Figure 8.1: *Systematic shift (horizontal lines) and measurement resolution (error bars) of* x_B*,* E_{jet}*,* Θ_{jet} *and* p^2_{Tjet}/Q^2 *in selected bins.*

Due to the limited statistics of the data, we try to minimize the number of bins. Since we want to present the forward jet cross-section as a function of x_B we have to choose more bins in this variable. For other variables we usually select three bins only – just to be able to control migrations to and from the interesting area. Bin widths are chosen to be larger than measurement resolution. Fig.8.1 shows resolution – plotted as error bars, and systematic shift – given by horizontal lines, of x_B, E_{jet}, Θ_{jet}, p_{Tjet}^2/Q^2 in selected bins.

To check how big migrations from bin to bin are, we define two variables:

- efficiency ($\mathcal{E}$) – probability to find a detector level jet in the same bin where a hadron level jet was generated
$$\mathcal{E} = \frac{N(DJ \wedge HJ)}{N(DJ)} , \tag{8.6}$$
where $N(DJ \wedge HJ)$ denotes the number of jets generated and detected in a given bin, and $N(DJ)$ corresponds to the number of jets detected in this bin,
- purity ($\mathcal{P}$) – probability to find a hadron level jet in the same bin where a detector level jet was measured
$$\mathcal{P} = \frac{N(DJ \wedge HJ)}{N(HJ)} , \tag{8.7}$$
where N(HJ) corresponds to the number of hadron level jets generated in a given bin.

Fig.8.2 illustrates efficiency and purity of the forward jet sample as seen in the MEPS and CDM Monte Carlo models. The graph shows total numbers of events containing hadron, detector, or both hadron and detector level jets fulfilling all selection conditions.

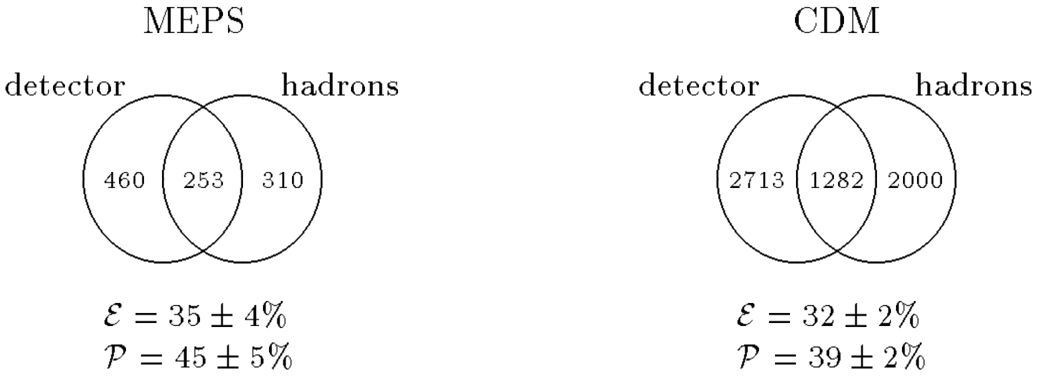

Figure 8.2: *Illustration of forward jet migrations, obtained with the help of the CDM and MEPS MC models. Numbers correspond to the number of events which contain detector, hadron, or both detector and hadron level jets.*

As one can see, less than a half of the events originating from the interesting kinematical area are detected in this area, and most of the events containing a measured jet fulfilling all cuts do not contain an appropriate hadron level jet.

Fig.8.3 shows how purity and efficiency change for different x_B bins.

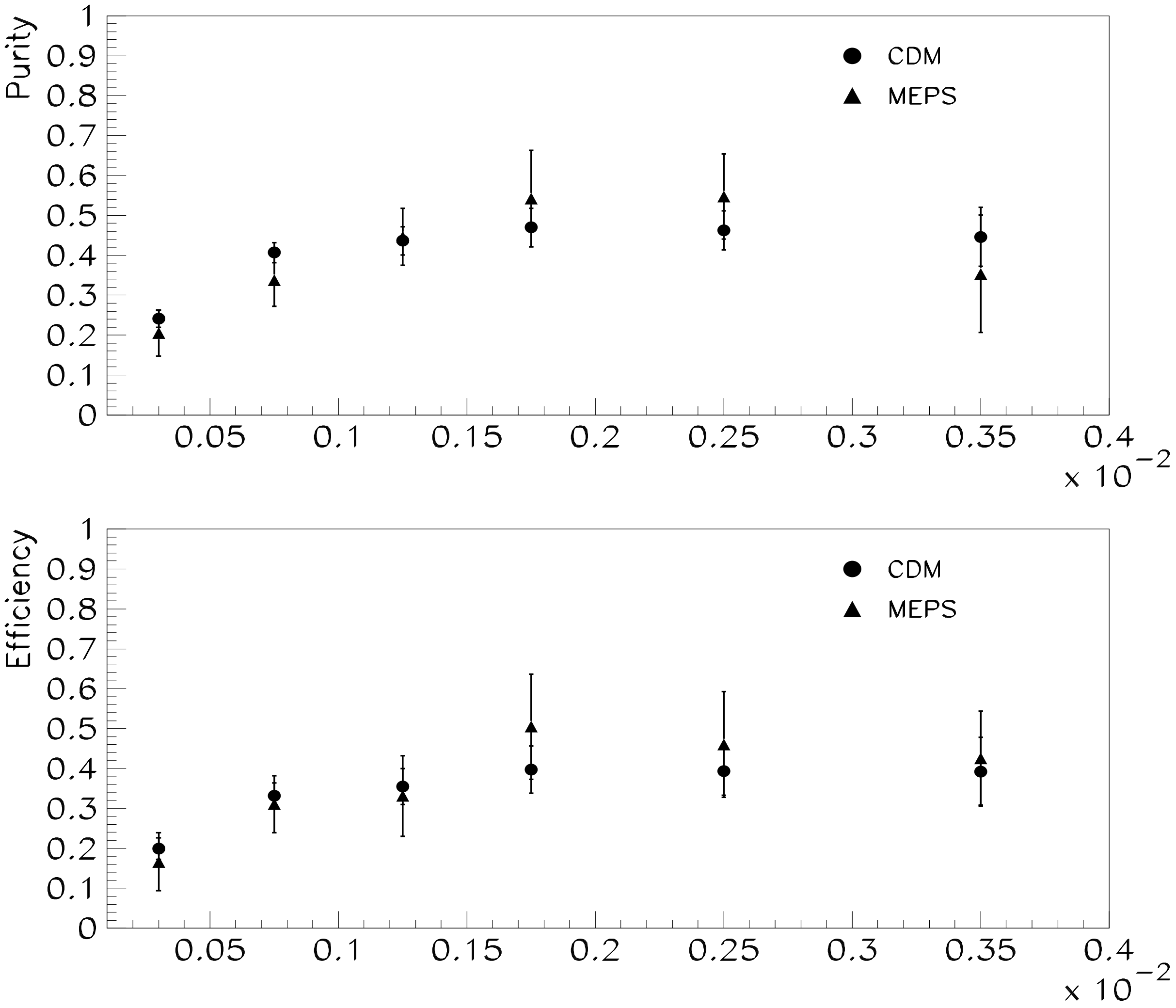

Figure 8.3: *Efficiency and purity for different x_B bins – shown for two MC models.*

Both purity and efficiency drop for the lowest and highest x_B bins.

As seen in Figs.8.2, and 8.3, forward jet measurement suffers from very high migrations, so the unfolding procedure is an important part of this analysis.

8.2.2 Tests of the Bayes unfolding method

The unfolding program used in this analysis consists of two parts:

- kernel of the unfolding procedure – written by G. D'Agostini – a short, self-contained code in Fortran based on the scheme described in Section 8.1,
- code that reads MC and data files, constructs multidimensional matrices, prepares input for the D'Agostini's procedure, and – if required – smoothes the results of the unfolding before feeding them into the next step, estimates and subtracts the background, makes statistical and systematic error calculations, provides final his-

tograms and numerous control plots. It is implemented in a quite long (about 2000 lines) Fortran code and was written for the purposes of this analysis.

Several tests have been run to check if the unfolding program produces correct results. The most significant ones are presented here.

For the main test of the unfolding method we use two Monte Carlo models. We construct the transformation matrix using one model, while the other one is used as "real data" we want to unfold. We check if the unfolding procedure is able to find back the true distribution (hadron level) of the Monte Carlo model used as the "real data".

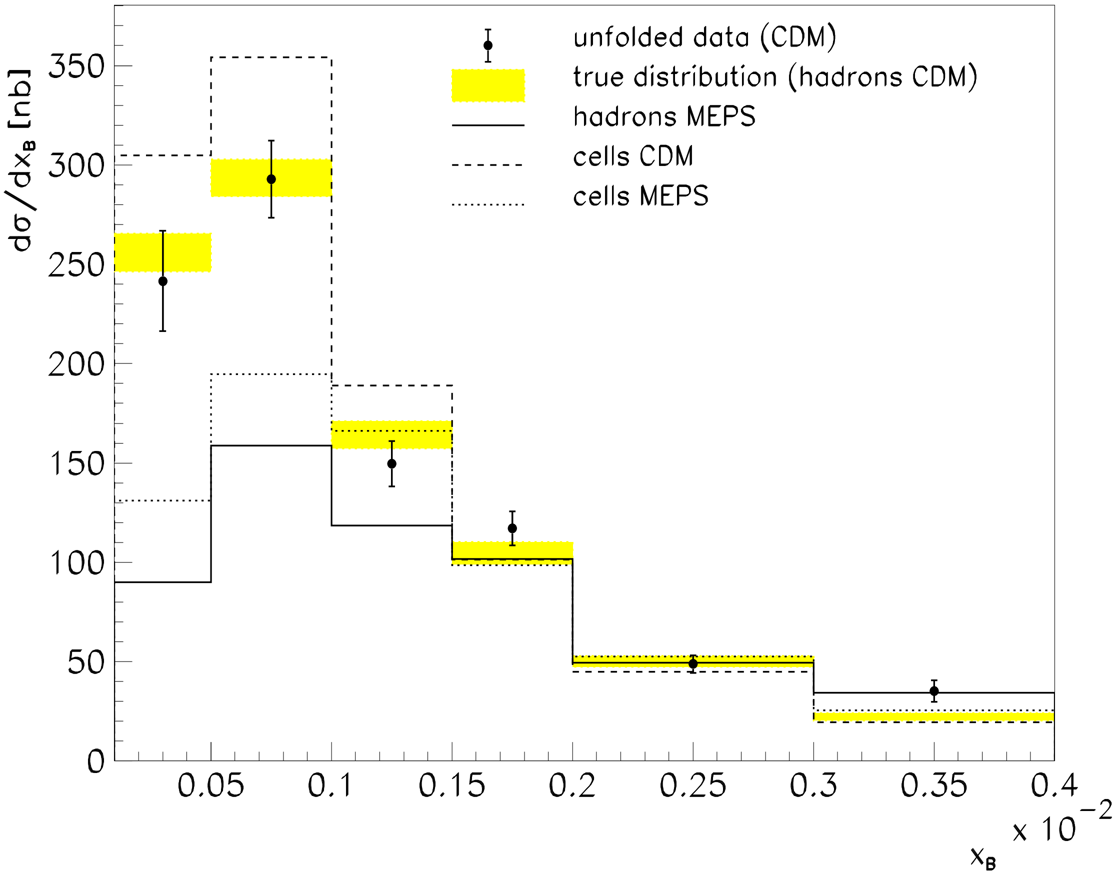

Figure 8.4: *Results obtained by 2-step unfolding. Transformation matrix based on the MEPS model is used to unfold the CDM detector (cells) data in order to get back its true (hadron) level.*

The x_B distribution is shown in Fig.8.4. Shaded band represents the CDM hadron level with statistical uncertainties – it is the true distribution for our test. Black points indicate the unfolded distribution with its statistical errors. Dashed and dotted lines display distributions of the CDM and MEPS detector levels, respectively. Solid line shows the MEPS hadron level. We draw hadron and cells (measured) levels for both of these Monte Carlo models just to illustrate how much the models differ from each other.

One may easily notice that the unfolding procedure is able to correct detector level data in such a way that – within statistical errors – the hadron level is restored.

Other tests carried out to check correctness of the unfolding method examine stability of the results with increasing number of steps and with varying number of bins and dimensions the procedure is performed in. These checks show that variations of the number of bins and dimensions do not change the results of unfolding, i.e. results after variation are consistent with the standard ones within statistical errors. A reasonable increase in the number of iterations also creates results that agree quite well with the true distributions. However, performing too many iterations of the unfolding procedure produces a strongly fluctuating solution. The reason for this behaviour is that every bin of the true distribution acts as an independent degree of freedom and after a very large number of iterations a kind of amplification of statistical fluctuations is reached [28].

8.2.3 Comparisons of results of the Bayes and the bin-to-bin unfolding methods

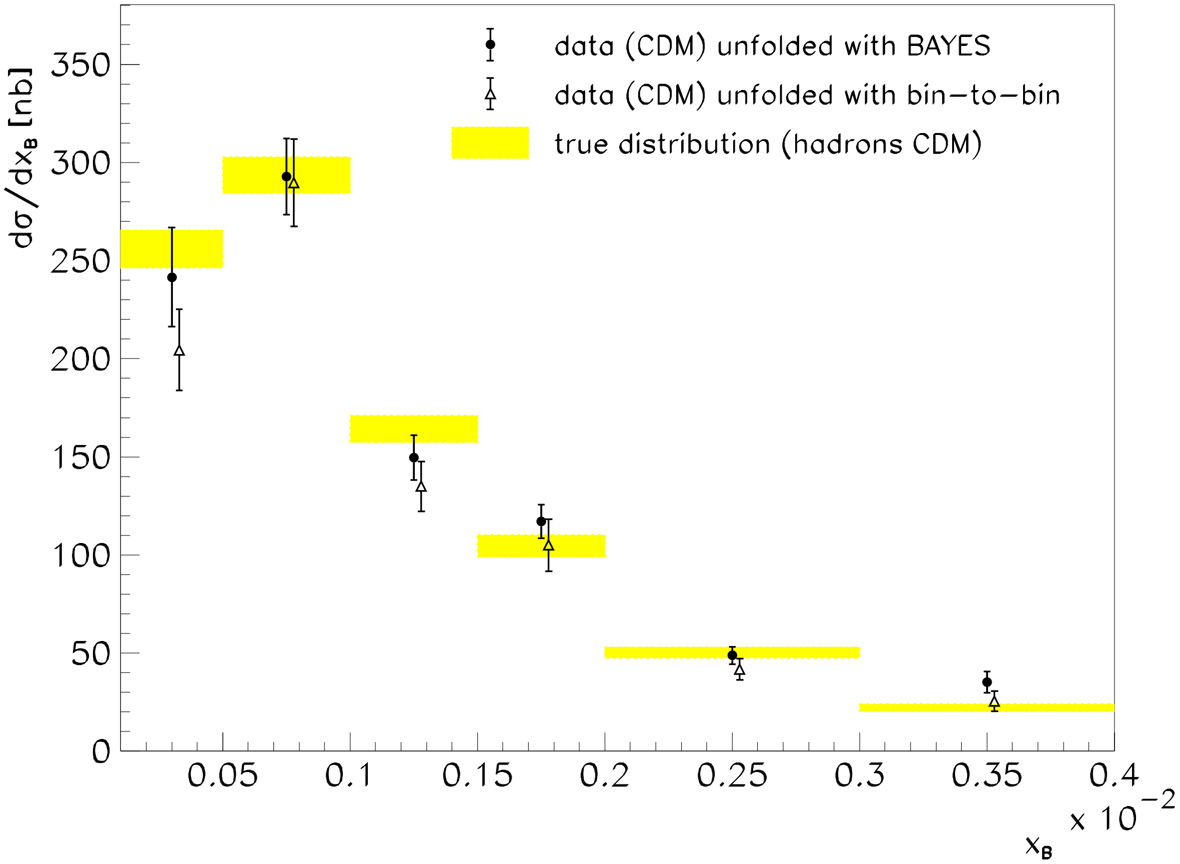

Figure 8.5: *Comparison of the Bayes and bin-to-bin unfolding procedures. Both methods are based on the MEPS MC and try to correct the CDM detector (measured) level data to the hadron (true) level.*

Results of the Bayes unfolding are compared to those obtained with the bin-to-bin method. As previously, we use the MEPS MC model to correct the CDM detector level data to the true (hadron) level.

In Fig.8.5, results obtained with both unfolding methods are shown. Shaded band illustrates the true level with its statistical uncertainties, while the results of the Bayes unfolding are drawn with black points and the bin-to-bin results are depicted with empty triangles. Error bars indicate statistical errors.

The bin-to-bin and Bayes unfolding methods give results compatible within statistical errors. However, in most bins the Bayes procedure points exhibit a better agreement with the true distribution than the bin-to-bin ones. To make a comparison between the true level and the two unfolded distributions, the χ^2 test is used:

$$\chi^2 = \sum_{i=1}^{N\,bins} \left(\frac{y_i - y_{i\,true}}{\delta_i}\right)^2 \tag{8.8}$$

where y_i represents the contents of the *i-th* bin of the unfolded distribution, $y_{i\,true}$ – the contents of the *i-th* bin of true distribution, and δ_i corresponds to the error of the *i-th* bin. We compare distributions which have 6 bins, i.e. 5 degrees of freedom. We get $\chi^2 = 4.81$ for the Bayes unfolding procedure and $\chi^2 = 6.42$ for the bin-to-bin one, so both methods can provide quite good approximations of the true distribution.

By the way, let us note that the bin-to-bin method is very sensitive to the agreement between the data and MC distributions of all parameters affected by the cuts. For example, when we use a different MEPS version (Lepto6.4) for the unfolding, the results of Bayes method are almost unchanged, but the results of the bin-to-bin method drop significantly (up to 30% in the low x_B bins). The reason for this behaviour is the fact, that Lepto6.4 does not describe all jet parameters quite well, but still provides an accurate description of detector effects. So the Bayes unfolding may work properly (the transformation matrix is correct), but the bin-to-bin method is unable to find the true results.

Real data distributions corrected to the hadron level with the use of the Bayes and bin-to-bin unfolding methods also produce results which agree with each other within statistical errors [30].

8.2.4 Calculation of statistical errors for the Bayes unfolding method

For the bin-to-bin unfolding, calculation of statistical uncertainty is straightforward. Statistical errors for both the uncorrected data and the Monte Carlo model distributions are estimated as the square root of the number of events in each bin. Statistical uncertainties of the corrected data are then determined using standard error propagation calculations.

Calculation of statistical errors including not only the uncertainties coming from limited statistics of the data and MC events, but also the effects of bin to bin migrations in an iterative unfolding procedure is a more complex problem. D'Agostini's unfolding algorithm based on Bayes' Theorem allows one to calculate statistical errors. However, the CPU time needed for the calculation diverges like the number of bins to the fourth power, and if there are many bins (which is the case in our analysis) a couple of weeks of the CPU time would be necessary to compute statistical uncertainties. Therefore, we have to evaluate the errors in a different way.

We vary uncorrected data and the Monte Carlo transformation matrix within their statistical errors and we measure the effect this change has on the corrected distribution.

In order to make the variation, a random number generator is used. The generator gives random numbers according to a Gaussian distribution with mean value x and variance σ^2. Each bin in the data and the Monte Carlo transformation matrix is varied separately by setting both x and σ^2 equal to the nominal number of entries in the bin. The number generated is taken as a new population of the bin. For bins where the number of entries is very low (5 or less), the Poisson distribution is used. When the populations of all bins are varied the unfolding procedure is performed to find the corrected distribution. We repeat this procedure one hundred times to produce one hundred different corrected distributions. Statistical errors are then calculated as the root mean squared deviation in each bin of the corrected distribution from the nominal one.

To demonstrate that one hundred varied corrected distributions are sufficient to obtain a good estimate of statistical errors, in Fig.8.6 we show the calculated value of the statistical errors as a function of the number of corrected distributions used in their determination. Each of the pictures in Fig.8.6 corresponds to one of the bins of the unfolded distribution.

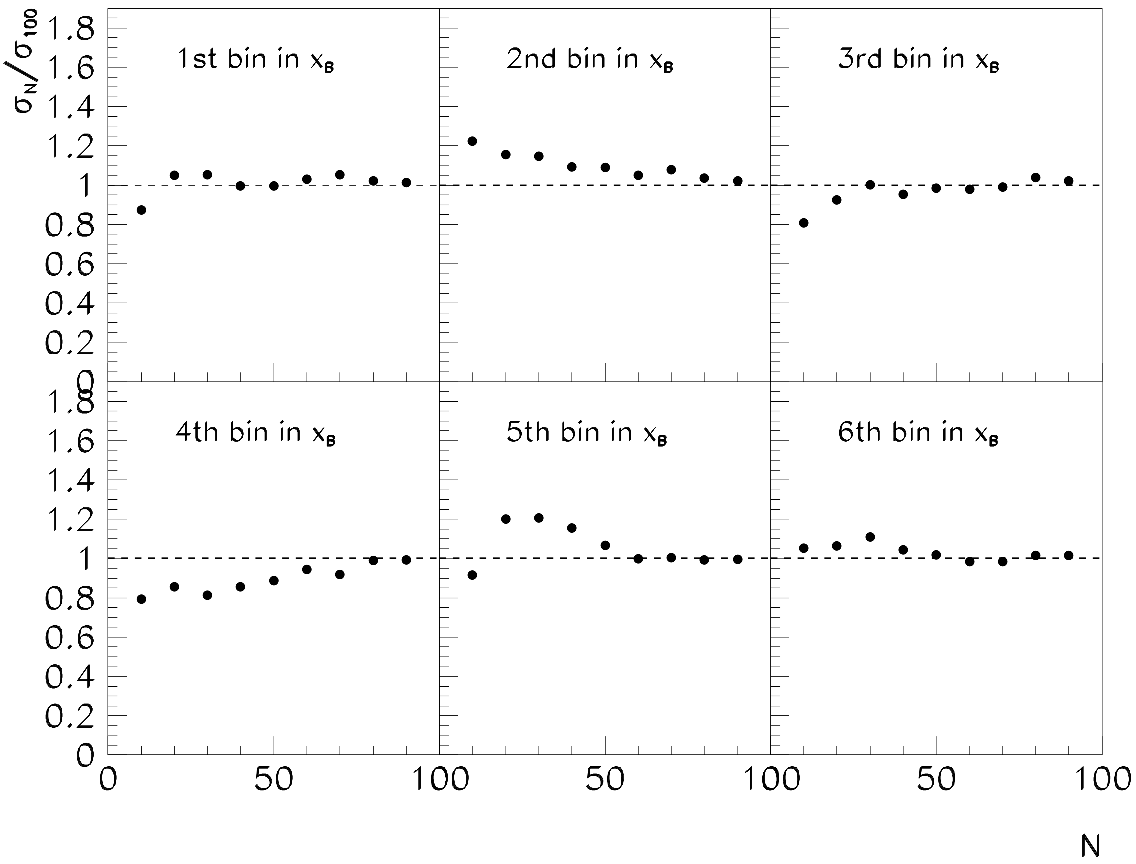

Figure 8.6: *Relative value of statistical uncertainty for six x_B bins as a function of the number of corrected distributions used in their determination.*

As the number of corrected distributions increases, the value of the statistical error converges levelling off after about eighty corrected distributions.

The method of estimating statistical errors described above is very similar to B. Efron's "bootstrap" technique [29] known to be very successful in solving various statistical problems.

We have checked for distributions with limited number of bins that error bars found using the above method are not smaller than error bars calculated using the method implemented in the unfolding code.

8.2.5 Systematic uncertainties

Monte Carlo models are able to describe all detector effects with a limited accuracy, so there are ambiguities concerning the choice of the transformation matrix. One has to try all possible transformation matrices in order to evaluate their systematic effects on the results. The main uncertainties which may have some influence on the final results are:

- uncertainty in the electron energy scale – 1% in the BEMC,
- uncertainty of the electron polar angle measurement – up to 1 mrad,
- uncertainty in the hadronic energy scale – determination of this source of error is based on the study of the transverse momentum balance $p_{T,h}/p_{T,e}$ ($p_{T,h}$ is hadronic transverse energy and $p_{T,e}$ – electron transverse energy) in the forward region. This analysis permitted assignment of a 4% error on hadronic energy deposited in the LAr calorimeter (the same hadronic energy scale uncertainty is found for hadronic energy deposited in the central LAr calorimeter). Fig.8.7 shows experimental and Monte Carlo distributions of the transverse momentum balance for all DIS events (a.) and for events selected with the forward jet cuts (Table 6.1) (b.).

For each source of the systematic error the analysis is repeated with transformation matrix modified appropriately. All contributions are added quadratically in order to find the total systematic error.

The main contribution to the total systematic error comes from uncertainty in the hadronic energy scale, and uncertainty in the electron position measurement gives a negligible contribution.

Systematic errors for each bin of the corrected distribution will be listed in the next section in Table 9.1.

Other sources of systematic errors are also considered, the main one being model dependence. Two different MC models (Django6 and Lepto6.5) are used to test how the results depend on the Monte Carlo model we use. It turns out (see Table 9.1) that differences between the results produced with the use of various models are well contained within statistical errors. This suggests that the discrepancies are due to statistical fluctuations[10] rather than to a systematic effect.

Nevertheless, we add a 2% systematic error to account for the MC model dependence. This 2% error comes from the difference between results obtained for the two models in the unfolding procedure with a minimal number of bins (only 3 bins in x_B), thus also

---

[10] It should be noted that statistics available for Lepto6.5 is quite limited.

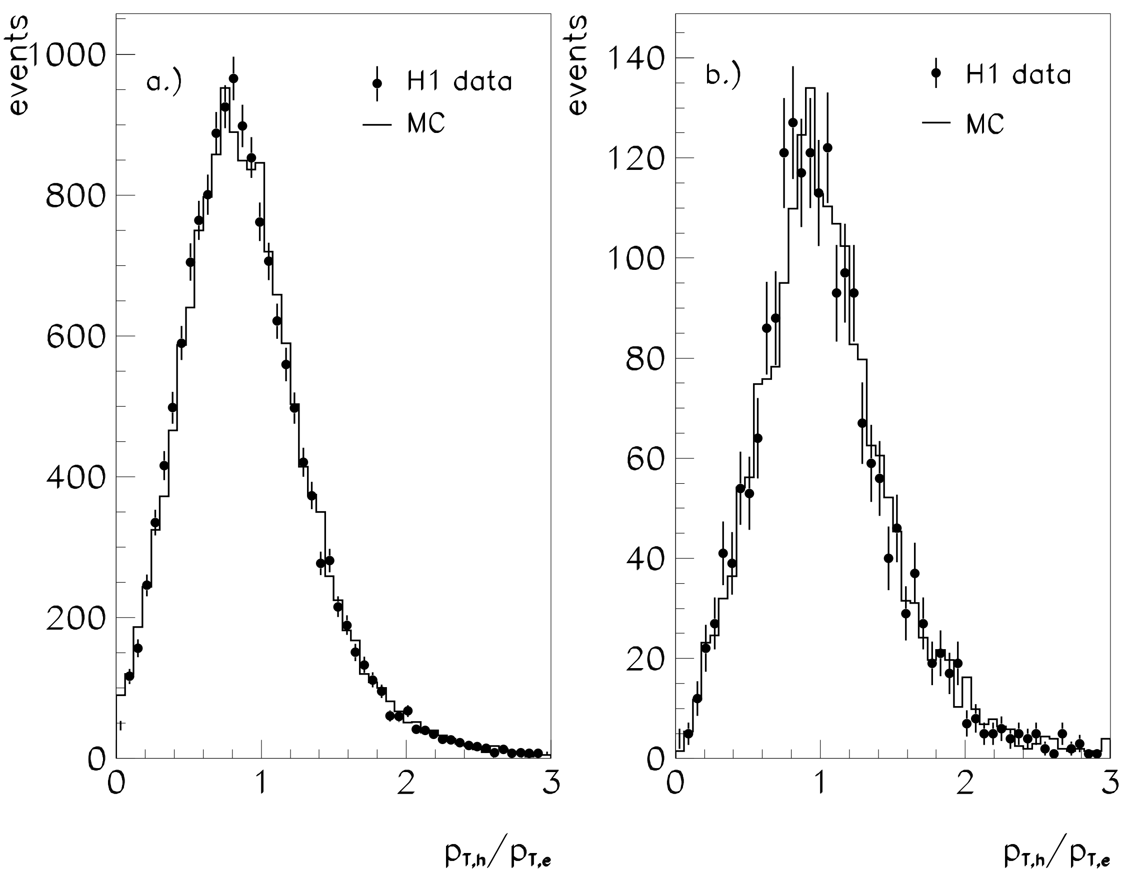

Figure 8.7: *Experimental and Monte Carlo distributions of the transverse momentum balance for all DIS events (a.) and for events selected with the forward jet cuts (b.).*

with minimized statistical fluctuations.

Precision of luminosity measurement introduces an additional 1.5% error to the analysis of the cross–section.

9 Results

9.1 Forward jet cross–section as a function of x_B.

Final values of the forward jet cross–section measurement along with the statistical and systematic errors are listed in Table 9.1. For data correction the CDM MC model is used because of the highest statistics available. However, to demonstrate that other models give results compatible within statistical errors, the values for data corrected with the MEPS MC model are also tabulated.

x_B bin	$d\sigma/dx_B$ [nb] (CDM used)	stat. error	sys. error up	sys. error down	$d\sigma/dx_B$ [nb] (MEPS used)	stat. error
(0.0001,0.0005)	199.3	12.3	22.3	7.8	188.5	24.0
(0.0005,0.001)	337.6	15.8	47.0	24.0	354.6	24.8
(0.001,0.0015)	218.6	13.4	40.0	22.6	193.8	17.8
(0.0015,0.002)	147.4	11.0	25.4	16.8	156.4	16.6
(0.002,0.003)	73.5	6.7	16.0	9.3	72.6	9.9
(0.003,0.004)	38.7	4.9	9.4	7.8	56.5	11.5

Table 9.1: *Final results of the measurement of the forward jet cross–section in the x_B bins. Values of the cross–section for data corrected with the CDM and MEPS Monte Carlo events are shown. (Note that we present the results as $d\sigma/dx$, so the cross–section is divided by the x_B bin width and integrated over all other variables in the area allowed by the forward jet cuts (see Table 6.1).)*

The forward jet cross–section for the corrected data is compared to the results of the Monte Carlo models and to the predictions of theoretical calculations.

Fig.9.1 shows the forward jet cross–section, as measured in the given x_B bin and divided by the bin width, for the kinematical and jet cuts defined in Table 6.1. Corrected data (indicated with black points) are compared to the predictions of the MC models (shown with different lines). The errors depicted are statistical (inner error bars) and systematic errors added in quadrature.

The data exhibit a steep rise with decreasing x_B. The MEPS model is too low and too flat to describe the data. The CDM model is slightly below the data but follows the shape. Let us stress again that the CDM model, in contrast to the LO–DGLAP model (MEPS), does not include a p_T–ordered cascade, which makes this model more similar to the BFKL scheme.

Fig.9.2 illustrates the forward jet cross–section as a function of x_B compared to the predictions of analytical calculations. Theoretical predictions are derived at parton level. The calculation labeled “Born” corresponds to the Born approximation for the forward jet process (see Section 3.1). The BFKL calculations are based on asymptotic expressions derived from the BFKL equation. We show two independent BFKL results: “BFKL Bartels” [31] and “BFKL Durham” [32]. There are some differences between these two approaches. The Bartels group uses the fixed coupling constant in the BFKL equation, while the group from Durham performs the calculations with the running coupling constant. However, the main difference is in the starting point of the BFKL evolution. In

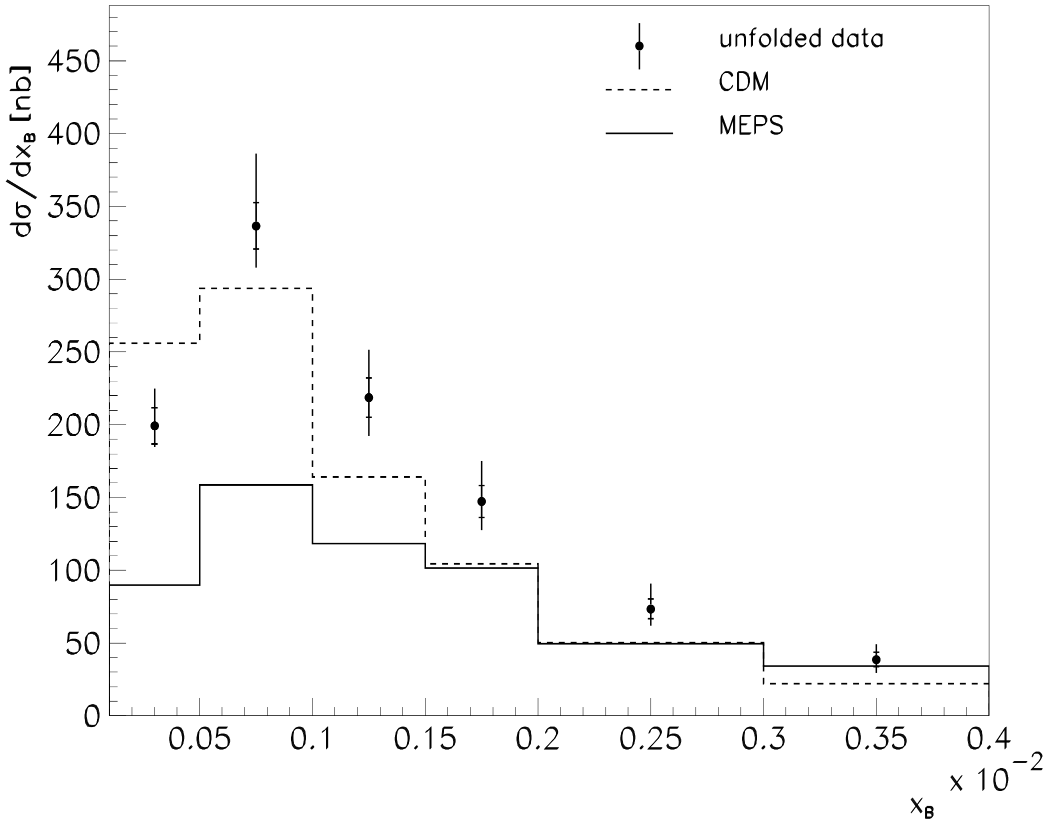

Figure 9.1: *Forward jet cross–section as a function of x_B. The cross–section is divided by the x_B bin width and integrated over all other variables in the area allowed by the forward jet cuts. Black points indicate corrected data. Statistical (inner error bars) and systematic errors are added in quadrature. Predictions of the MC models are shown with different types of lines.*

the calculations the BFKL evolution starts at some $z = x_B/x_{jet}$, where BFKL effect is expected to be small and evolves down in z. The Bartels group begins the evolution at $z_0 = 1$ and the Durham group begins it at $z_0 = 0.12$. In some sense, by choosing the suitable value for the starting point, normalization of the Durham results is fitted to the data.[11] Nevertheless, the shape remains unchanged, so the accuracy of this prediction may be judged from the comparison of the slopes.

The Born prediction is much too low and too flat to agree with the data, the "Bartels BFKL" points are more in accord with the data, though the slope seems too steep. The "Durham BFKL" results describe the shape of the data remarkably well.

However, one cannot draw any final conclusion because the data are corrected only to hadron level while the BFKL calculations give predictions at the parton level. One may

---

[11] The present strategy of the Durham group is to choose the starting point in such a way that normalization of their predictions agrees with the data. Using this normalization they are able to make a successful prediction not only of the shape of the forward jet cross–section, but also of the p_T spectra measurement.

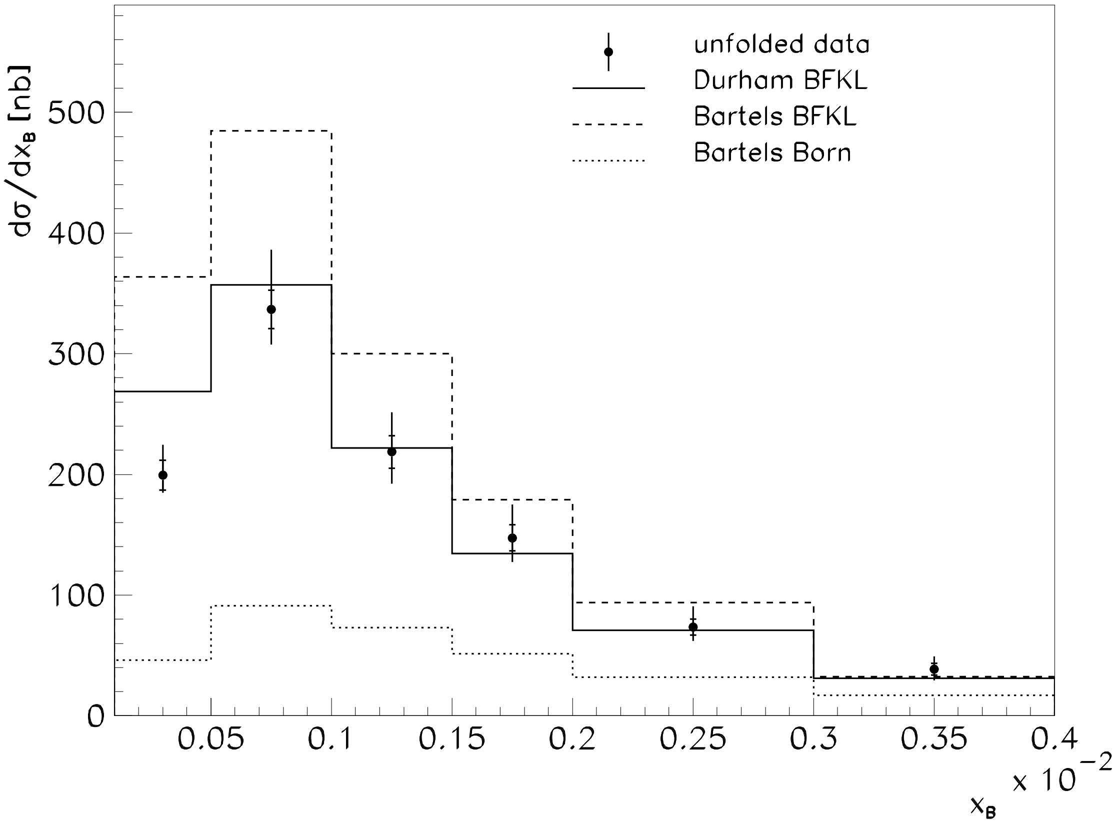

Figure 9.2: *Forward jet cross–section as a function of x_B. The cross–section is divided by the x_B bin width and integrated over all other variables in the area allowed by the forward jet cuts. Black points indicate corrected data. Statistical (inner error bars) and systematic errors are added in quadrature. Analytical predictions are shown: "Bartels Born" (the quark box diagram)– dotted line, "Bartels BFKL" (based on the BFKL evolution equation) – dashed line, "Durham BFKL" (based on the BFKL evolution equation) – full line.*

speculate, however, that in the case of the high–energy parton jet its parameters should not be significantly affected by hadronization.

We have tried to estimate distortions caused by hadronization. However, it has turned out that corrections for hadronization effects depend strongly on the Monte Carlo model used in the analysis. Fig.9.3 shows the correction factor for transition from the hadron level to the parton level as a function of x_B. The correction factor is defined as a ratio of the number of the DIS events with a parton level forward jet found in a given x_B bin to the number of the DIS events with a hadron level forward jet produced in the same bin. Results for the CDM and MEPS MC models are presented. Predictions of the CDM model confirm our expectations that these effects are not very significant (<20% in all but the highest x_B bin); however, the MEPS model shows that one may have distortions of 50% or higher.

Since hadronization effects seem to depend strongly on parton configurations[12], in order to make some definite statements concerning agreement between the data and the

---

[12] Note that both of the MC models use the same hadronization program – JETSET.

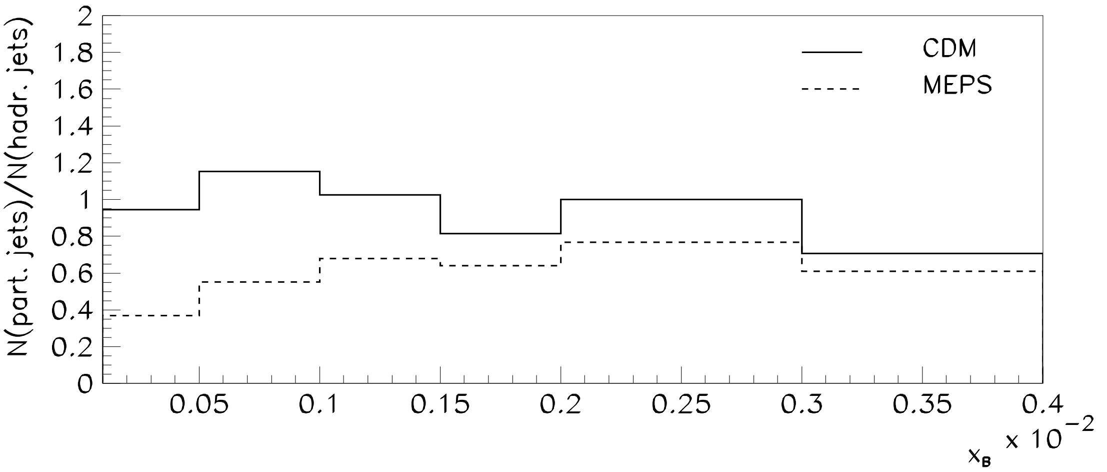

Figure 9.3: *Hadronization correction factor as a function of x_B for the CDM and MEPS Monte Carlo models.*

theoretical calculations, the BFKL predictions transformed to the hadron level are needed. For this task the BFKL Monte Carlo program or theoretical estimations of the parton ↔ hadron corrections for the BFKL case are necessary. Yet, these tools are still unavailable.

9.2 Forward jet cross–section as a function of x_B for different $p_{T_{jet}}$

We check how the forward jet cross–section changes with increasing $p_{T_{jet}}$ cut. Fig.9.4 shows the forward jet cross–section as a function of x_B for the following $p_{T_{jet}}$ cuts:
$p_{T_{jet}} > 3.5$ GeV, $p_{T_{jet}} > 5$ GeV and $p_{T_{jet}} > 6$ GeV. Due to limited statistics, especially for $p_{T_{jet}} > 6$ GeV, we present the cross–section in 2 bins in x_B only.

One may see that with increasing $p_{T_{jet}}$ the slope becomes smaller. It is not surprising, since the cut $0.5 < p_T^2/Q^2 < 2$ demands also higher Q^2 for higher $p_{T_{jet}}$, and for higher Q^2 the phase–space for low–x events is suppressed (Fig.6.3).
The data are above MC predictions for all $p_{T_{jet}}$ cuts.

9.3 Cross–section for two forward jets

We also measure the cross–section of events where two jets fulfilling all the forward jet cuts (see Table 6.1) were emitted. If there are two forward jets, they are usually radiated close to each other in polar angle θ but back-to-back in azimuthal angle ϕ so we do not have any problems with their separation.

Since we find very few such events (50 events in the data and 400 in all MC files), we use all available MC statistics (CDM + MEPS) for the unfolding. It is justified by the earlier analysis showing that these MC models give compatible results when used to correct for detector effects.

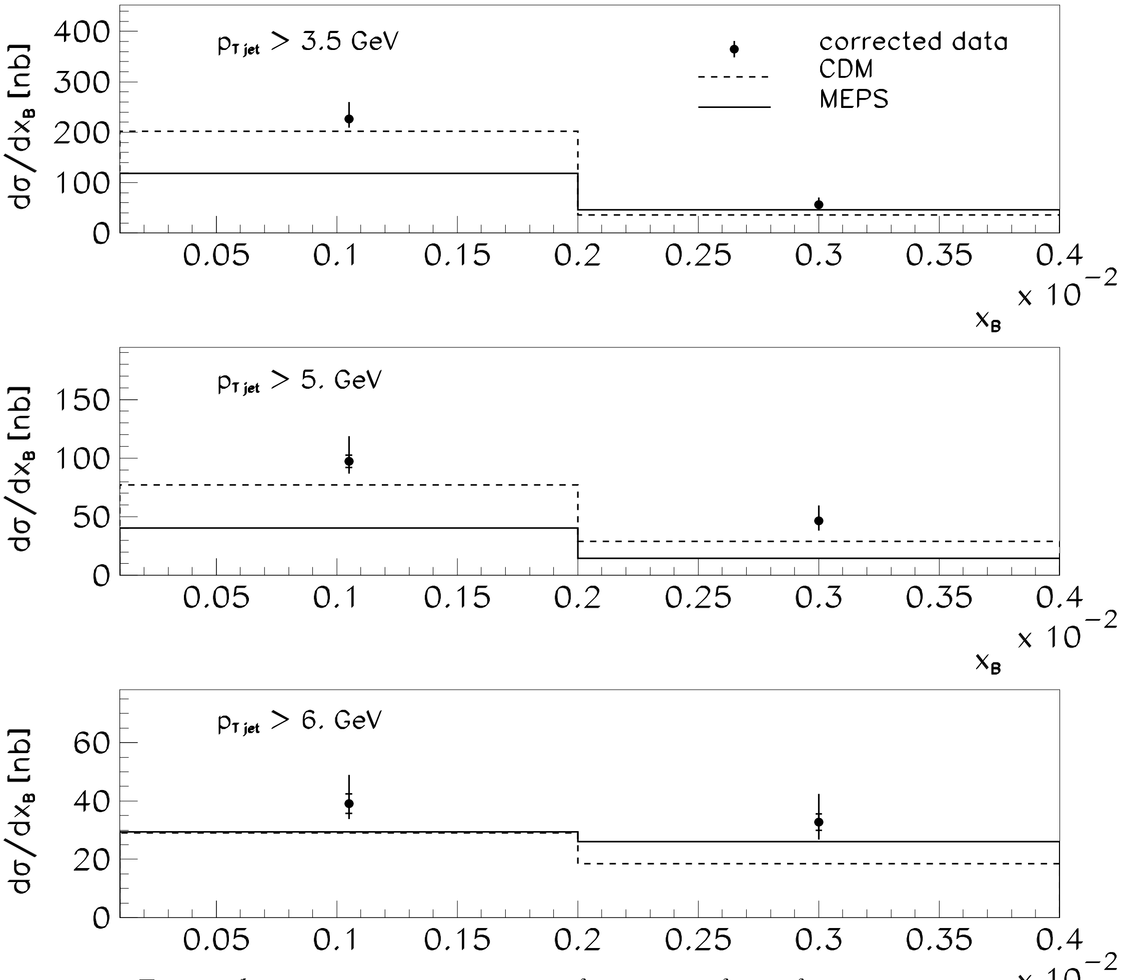

Figure 9.4: *Forward jet cross–section as a function of x_B for various $p_{T_{jet}}$ cuts. The cross–section is divided by the x_B bin width and integrated over all other variables in the area allowed by the forward jet cuts. Black points indicate corrected data. Statistical (inner error bars) and systematic errors are added in quadrature. Predictions of the MC models are shown with different types of lines (CDM – dashed line, MEPS – solid line).*

The corrected cross–section for the production of two forward jets is:

$$8.8 \pm 1.7\ ^{+4.3}_{-1.7}\ [pb]$$

Analytical calculations made by the Durham group predict [33] that for the kinematical region we use, the ratio of the cross–section for two forward jets production to the cross–section for one forward jet production is about 3%. Since we obtain the total cross–section for one forward jet production to be equal to:

$$540 \pm 16\ ^{+88}_{-43}\ [pb],$$

we should expect the cross–section for two forward jets production to be about 16 pb. This prediction exceeds our measurement by a factor of 2. However, in this case direct comparison of calculation results made at the parton level with the cross–section corrected to the hadron level is much less accurate than it was in the case of one forward jet. We find again that the expectations of hadronization effects differ very significantly for various MC models. We do not give the exact value of the correction factor because of the very limited MC statistics the studies were based on.

9.4 Cross–section of two forward jets for the relaxed upper p_T^2/Q^2 cut

In order to increase the statistics for the two forward jet measurement, we decide to relax the upper p_T^2/Q^2 cut. The upper limit is not essential for our analysis, since DGLAP evolution is suppressed by the lower p_T^2/Q^2 cut. We put $0.5 < p_T^2/Q^2 < 5$. We select 140 such events in the data.

Now the corrected cross–section for the production of two forward jets is:

$$27.8 \pm 4.3 \,^{+8.8}_{-2.6} \; [pb]$$

The cross–section for one forward jet production, with the relaxed p_T^2/Q^2 cut, is:

$$1000 \pm 23 \,^{+207}_{-109} \; [pb] \; ,$$

so the ratio of the cross–section for production of two forward jets to the cross–section for one forward jet production is 3%. For the relaxed cut, the theoretical calculations predict [33] the ratio to be about 6%, so again we have a difference by a factor of 2. And once more we have to stress that we do not know how big the hadron ↔ parton corrections are. The Monte Carlo studies are very inconclusive; the correction factor jumps from 0.36 ± 0.14 for the MEPS model to 2.2 ± 0.3 for the CDM model.

We can compare our data unfolded to the hadron level directly with the predictions of the MC models. We find that both the CDM and MEPS models predict similar cross–sections, 17 pb and 15 pb respectively, so the data exceed the MC predictions by a factor of 2.

9.5 Forward jet cross–section as a function of x_B for the relaxed upper p_T^2/Q^2 cut

For the relaxed upper p_T^2/Q^2 cut we also repeat the basic analysis. Now, the low–x_B region is less suppressed so the forward jet cross–section rises steeper with decreasing x_B. The corrected data compared to the MC models are shown in Fig.9.5 and the values of the cross–section and the errors are listed in Tab.9.2.

Let us point out that with the relaxed p_T^2/Q^2 cut also the Monte Carlo predictions rise steeper with decreasing x_B, so the relation between the signal (data) and the background (MC) stays almost the same.

x_B bin	$d\sigma/dx_B$ [nb]	stat. error	sys. error up	sys. error down
(0.0001,0.0005)	687.5	44.5	120.3	65.3
(0.0005,0.001)	612.4	24.6	113.2	54.4
(0.001,0.0015)	361.6	19.6	81.4	41.
(0.0015,0.002)	209.4	15.2	42.4	28.4
(0.002,0.003)	96.7	7.2	21.4	11.4
(0.003,0.004)	50.8	5.7	14.4	11.0

Table 9.2: *Final results of the measurement of the forward jet cross–section in the x_B bins for the relaxed p_T^2/Q^2 cut. We present the results as $d\sigma/dx$, i.e. the cross–section is divided by the x_B bin width and integrated over all other variables in the area allowed by the forward jet cuts. Statistical and systematic errors of the measurement are also listed.*

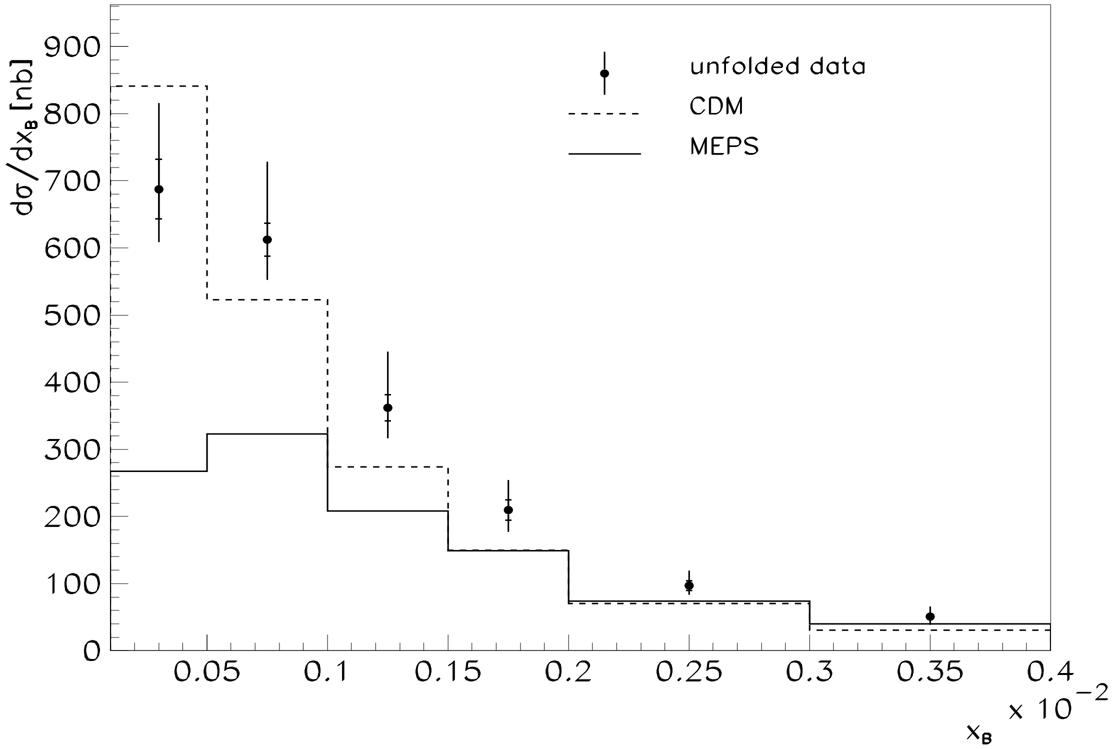

Figure 9.5: *Forward jet cross–section as a function of x_B for the relaxed upper p_T^2/Q^2 cut. The cross–section is divided by the x_B bin width and integrated over all other variables in the area allowed by the forward jet cuts. Black points indicate corrected data. Statistical (inner error bars) and systematic errors are added in quadrature.*

9.6 Comparison with the ZEUS results

In the ZEUS experiment the forward jet analysis is also carried out [34]. However, due to some disadvantages connected with their forward calorimeter (e.g. poor granuality) they have to rise the lower limit for Θ_{jet}, which automatically rises the low $p_{T_{jet}}$ cut. In order to get more statistics they relax the upper p_T^2/Q^2 cut. Other requirements are quite similar to those of our analysis. All of them are listed in Table 9.3.

$E_e > 10$ GeV

$0.0005 < x_B < 0.005$
$y_B > 0.1$

$p_{T_{jet}} > 5.$ GeV
$E_{jet} > 28.7 \text{ GeV} \Leftrightarrow x_{jet} > 0.035$
$\Theta_{jet} > 10.37^o \Leftrightarrow \eta_{jet} < 2.4$
$0.5 < p_{T_{jet}}^2/Q^2 < 4.$

Table 9.3: *Standard cuts for the forward jet analysis in ZEUS.*

In the ZEUS analysis the data are corrected to the parton level. The bin-to-bin method and the CDM (Ariadne 4.08) Monte Carlo model are used for the unfolding.

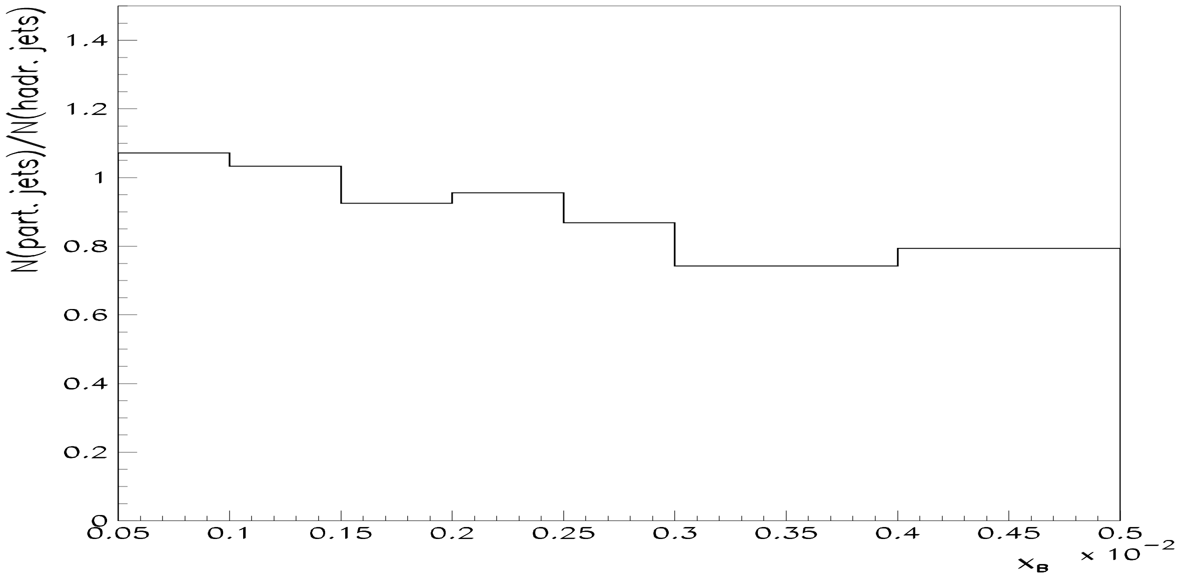

Figure 9.6: *Hadronization correction factor as a function of x_B for the CDM Monte Carlo model (Ariadne 4.08) and for the ZEUS cuts.*

In order to compare our data with the ZEUS results, we repeat the forward jet analysis using their cuts. We unfold our data only to the hadron level. However, Monte Carlo studies show that for Ariadne 4.08 Monte Carlo model and for the ZEUS cuts, the differences between the hadron and parton levels are not very significant (Fig.9.6).

Fig.9.7 shows the ZEUS [34] and H1 results. For comparison, predictions of the theoretical calculations and the Monte Carlo models are depicted.

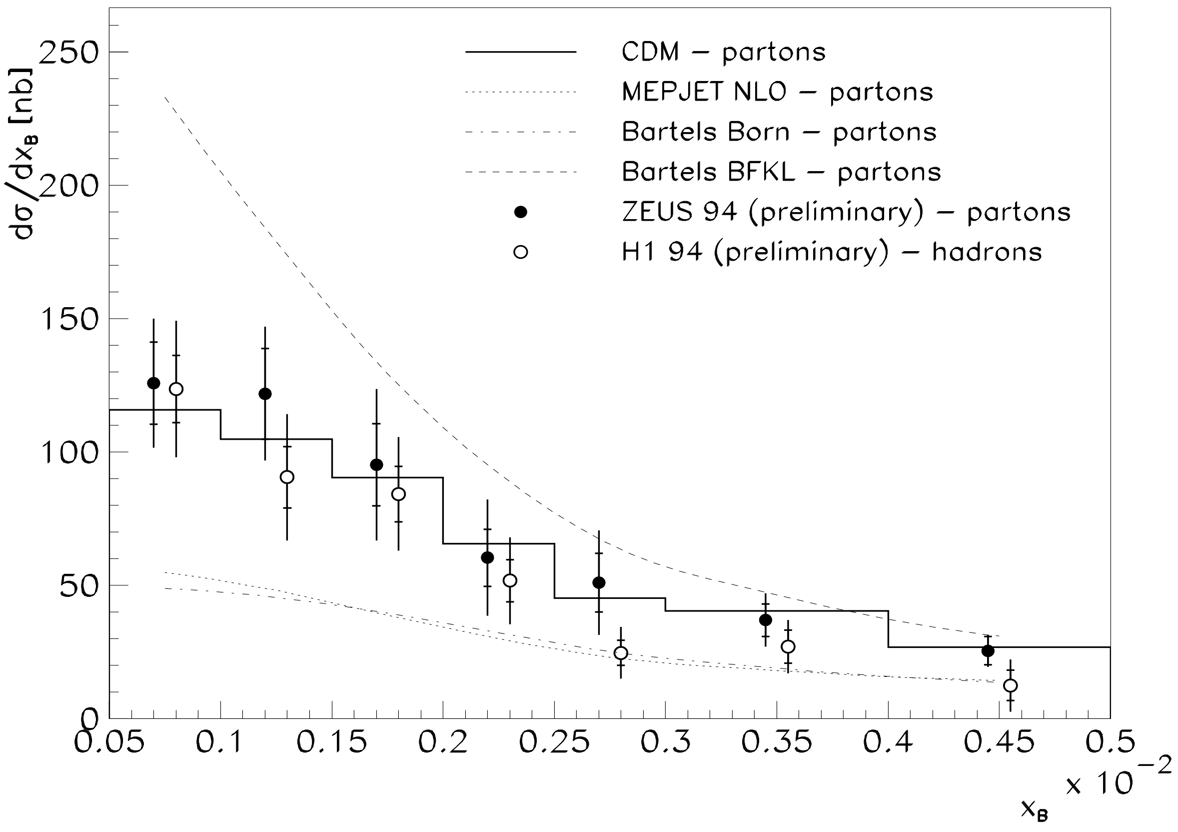

Figure 9.7: *Forward jet cross–section as a function of x_B. The ZEUS an H1 results are compared. Inner error bars correspond to statistical errors, the outer ones mark the total error. Predictions of analytical calculations and the Monte Carlo models are also shown. Note that the H1 results are unfolded only to the hadron level. Differences between the hadron and parton levels for the MC model and the cuts used for this analysis are of the order of statistical errors for the cross–section measurement.*

The ZEUS and H1 data do not show significant discrepancies. The CDM model reproduces the data quite well. For higher x_B bins the data agree also with the predictions of the fixed-order computations made with the MEPJET [35] MC model and with the Born calculations.

9.7 Correlations in the azimuthal angle between the forward jet and the outgoing electron.

We analyse also distribution of the forward jet cross–section as a function of $\Delta\phi$, where $\Delta\phi$ is defined as a difference in the azimuthal angle between the outgoing electron and the forward jet.

Fig.9.8 shows the differential forward jet cross–section ($d\sigma/d\Delta\phi$) as a function of $\Delta\phi$. The data are selected with the standard forward jet cuts (see Table 6.1).

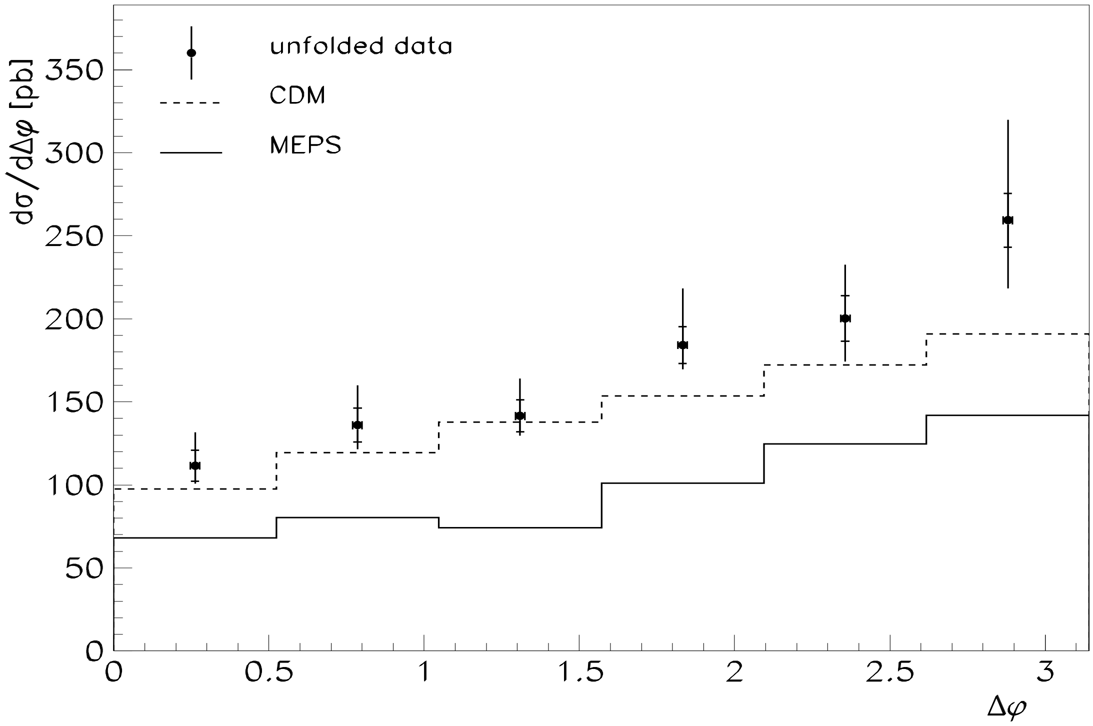

Figure 9.8: *Dependence of the differential forward jet cross–section ($d\sigma/d\Delta\phi$) on the azimuthal difference between the forward jet and the outgoing electron ($\Delta\phi$). Black points indicate corrected data. Statistical (inner error bars) and systematic errors are added in quadrature. Predictions of the CDM MC model are shown with dashed line.*

The cross–section rises with increasing $\Delta\phi$. This may be interpreted as a behaviour similar to the one shown in Fig.3.5(right) where results of fixed–order numerical calculations are presented. Resolution of our measurement does not allow us to observe the dip at π, so we only see the monotonously rising distribution. However, the shape of the measured cross–section may also be a result of simple kinematics that constrains the jet and the electron to be produced back-to-back.

We also check dependence of the correlations in ϕ on x_B. For this purpose we divide the data into two bins in x_B: $0.0001 < x_B < 0.001$ and $0.001 < x_B < 0.004$ – Fig.9.9.

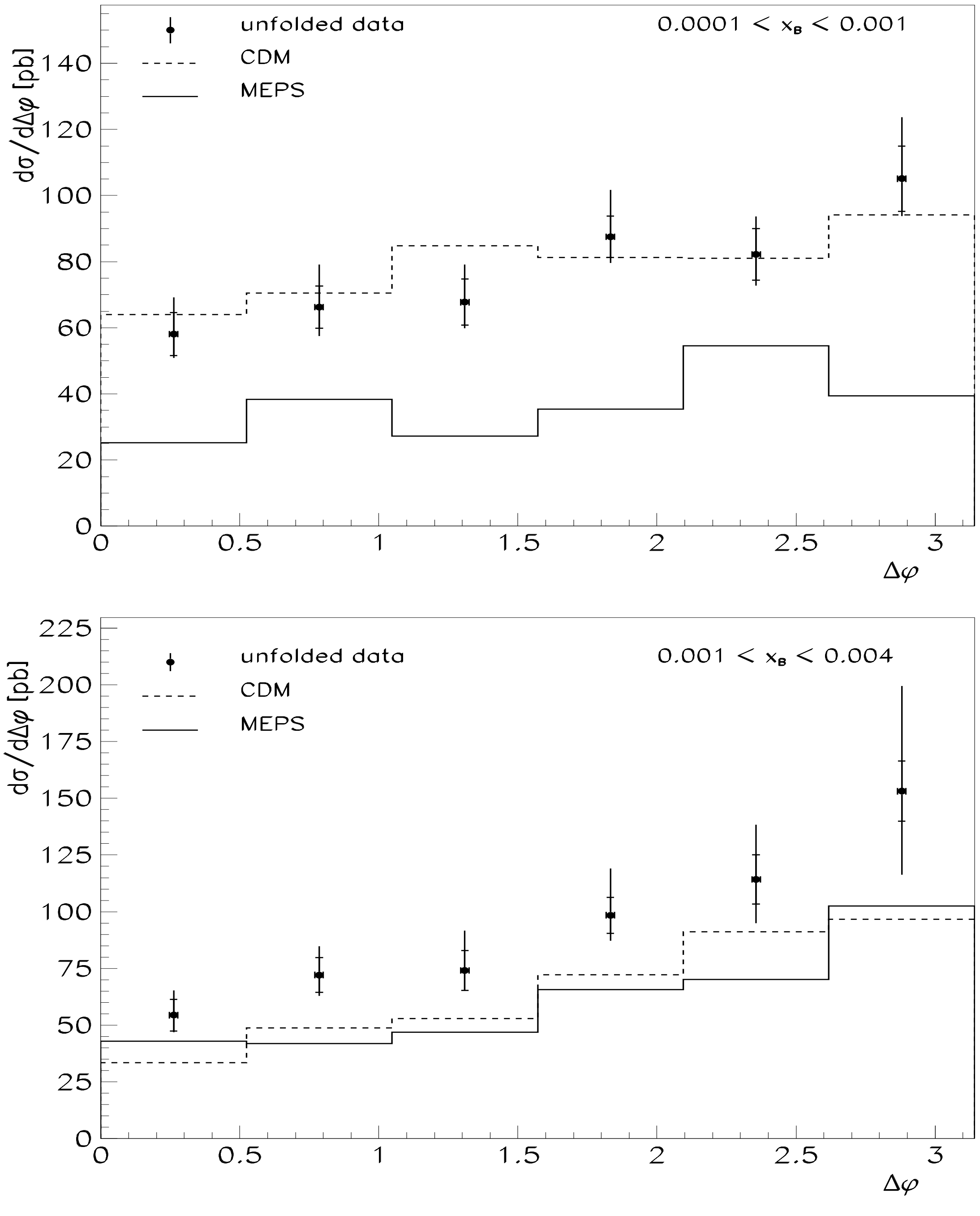

Figure 9.9: *Dependence of the differential forward jet cross–section ($d\sigma/d\Delta\phi$) on the azimuthal difference between the forward jet and the outgoing electron ($\Delta\phi$) for different x_B bins. Black points indicate corrected data. Statistical (inner error bars) and systematic errors are added in quadrature. Prediction of the CDM MC model is shown with dashed line.*

For high x_B we observe distribution rising steeply with increasing $\Delta\phi$, which – as already mentioned – is in agreement with the fixed–order QCD calculations. For low x_B the distribution is much flatter, which may be interpreted as an effect of BFKL dynamics.

Thus, the measured shapes of the cross–section as a function of $\Delta\phi$ for low and high–x_B samples seem to confirm theoretical expectations outlined in Section 3.2.

On the other hand, the observed distributions may be explained also in quite a simple way. For high–x_B very few partons are emitted and the momentum conservation law forces the electron and the forward jet to go back-to-back. With decreasing x_B the phase-space for partons emission increases, so the kinematical constraints are relaxed and the distribution in $\Delta\phi$ gets flatter.

The CDM model – which does not have dynamical correlations between the electron and the partons implemented – is able to reconstruct the slope of the data for both x_B bins quite well.

Summarizing, the study of azimuthal correlations between the outgoing electron and the forward jet does not lead to any definite conclusions. The interpretation is still open. We do not know how much hadronization blurs hypothetical correlations at the parton level. We cannot say whether dynamical correlations really exist in the measured data, or if everything we observe is just a consequence of phase space and kinematical constrains. More precise theoretical predictions and/or a measurement able to distinguish between the kinematical and dynamical effects are necessary.

Let us return for a moment to the DIS events containing two forward jets in a hadronic final state and analyse these events versus azimuthal correlations. In this case the kinematical bias should not be that significant. However, we suffer from low statistics, so we show only the rate of the raw measured events without any corrections to the hadron level. In Fig.9.10(a.) the difference in ϕ between these two jets is shown. The two forward jets tend to go back-to-back.

We check also the correlations in ϕ between the forward jets and the outgoing electron. In Fig.9.10(b.) distributions of $\Delta\phi$ for the first forward jet – the jet with the highest energy (black points), and the second one (empty points) are shown. We observe quite flat distributions for both forward jets, which is in agreement with the analytical calculations for BFKL dynamics. It is a promising result; however, it is shown here rather as an appetizer and an indication that with higher statistics and some new tools delivered by theoreticians (e.g. the BFKL Monte Carlo model, estimations of the hadronization corrections etc.) a lot may still be done in the field of the forward jets.

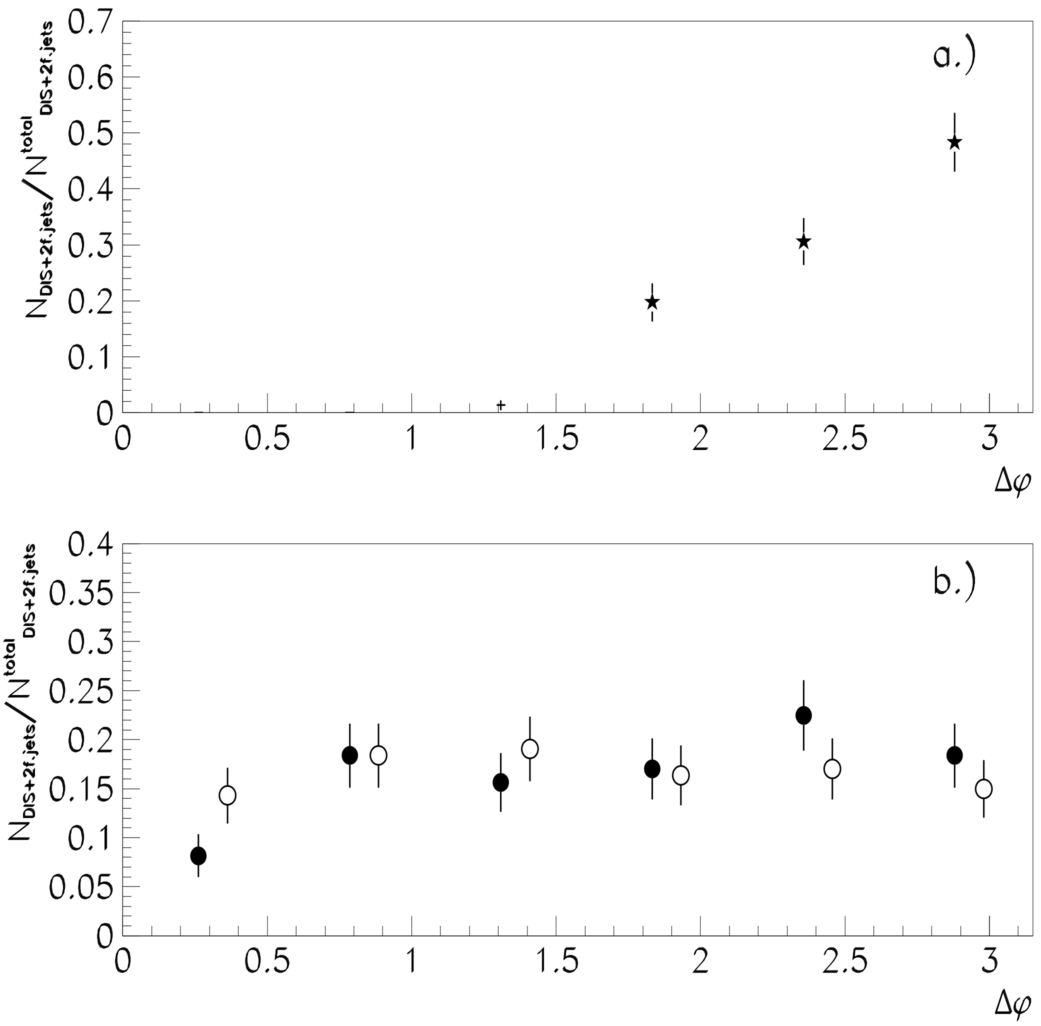

Figure 9.10: *Azimuthal angle correlations for the DIS + 2 forward jets events:*
(a.)$\Delta\phi$ *between the first jet and the second one,*
(b.)$\Delta\phi$ *between the first jet and the outgoing electron (black points), and the second jet and electron (empty points). Statistical errors are indicated.*

10 Summary

Measurement of forward jet production as a possible signature of BFKL dynamic has been presented. The analysis was based on full data sample (corresponding to 2.82 pb^{-1}) collected in 1994 in the H1 experiment.

DIS events containing, in the hadronic final state, a jet emitted close to the proton remnant direction were selected. In order to weaken the DGLAP evolution, the jet transverse momentum square was required to be of the order of the square of the four–momentum transfer and, with the purpose of maximizing the phase space for the BFKL evolution, x_{jet} much bigger than the Bjorken x_B was demanded. Some 2000 forward jet events were selected.

Complex jet studies were performed. Clear-cut jet profiles and the QCD – predicted dependence of the jet widths on jet transverse momenta show that the objects we are dealing with are well-defined jets.

The data were corrected for detector effects and reconstruction distortions by means of the Bayes unfolding. It was shown that for this analysis the Bayes unfolding gives results compatible with those obtained by the bin–to–bin method.

The main study was devoted to the measurement of the forward jet cross–section as a function of x_B. The results were compared with analytical calculations and the Monte Carlo models predictions. The MEPS model – the DGLAP based model – fails to describe the data both in normalization and shape. The CDM model – the model without parton transverse momenta ordering – is able to follow the shape of the data distribution quite well. Also, the Durham BFKL calculations are able to predict the slope of the data with high accuracy. The Bartels results show that the BFKL prediction is more in accord with the data than the calculations of the Born model .

We also studied the cross–section of the DIS + 2 forward jets events. We selected 50 such events with standard forward jet cuts, and 140 for standard cuts with the relaxed upper p_T^2/Q^2 limit. Results of our analysis fall below the predictions of BFKL calculations, but above the MC models expectations. The reasons for discrepancies between BFKL calculations performed at the parton level and the data which are corrected only to the hadron level may be due to hadronization effects.

The ZEUS collaboration has recently reported their results of the DIS+1 forward jet cross-section measurement. So as to compare our results with theirs, we repeated our analysis using their cuts. Distributions of the DIS + 1 forward jet cross–sections for the ZEUS and H1 data show quite good agreement.

We analysed the distribution of the azimuthal angle between the outgoing electron and the forward jet. We observe that this distribution is quite flat for the low–x_B sample, while for higher x_B it exhibits a significant rise towards 180°. The behaviour for low–x_B is

in agreement with BFKL calculations and high x_B distribution may be described by fixed-order QCD calculations. However, shape of these distributions may be also explained by kinematics and phase space effects, so interpretation is still open.
Analysis of the DIS+2 forward jets events versus azimuthal correlations shows that the two forward jets are mainly produced back-to-back and the distributions of the azimuthal angle between the forward jet and the outgoing electron are quite flat for both the forward jets. This result is very promising, but preliminary – since it is based on very low statistics – and is rather supposed to be an appetizer for further forward jet analysis.

Summarizing, all processes investigated in this analysis show better agreement with BFKL predictions than those based on fixed–order or DGLAP calculations. Nevertheless, one cannot claim to observe clear signatures of the BFKL dynamics. Final conclusions will be possible only when direct comparison of the data with BFKL predictions becomes possible at the same level. For this purpose, Monte Carlo model based on the BFKL evolution equation or theoretical estimations of hadronization effects in the BFKL case are necessary.

Bibliography

[1] J. D. Bjorken, E. A. Paschos, *Phys. Rev.* **185** (1975).

[2] V. N. Gribov, L. N. Lipatov *Soviet J. Nucl. Phys.* **15** (1972) 438.
G. Altarelli, G. Parisi *Nucl. Phys. B* **126** (1977) 298.
G. Altarelli, *Phys. Rep.* **81** 1.

[3] Yu. Dokshitzer, *Soviet Phys. JETP* **46** (1977) 641.

[4] E. .A .Kuraev, L. N. Lipatov, V. Fadin, *Soviet Phys. JETP* **45** (1977) 199.
Ya. Ya. Balitskij, L. N. Lipatov, *Soviet J. Nucl. Phys.* **28** 822.

[5] H1 Collaboration, S. Aid et al., *Nucl. Phys.* **B 470** (1996) 3.
ZEUS Collaboration, M. Derrick et al., *Z. Phys.* **C 72** (1996) 399.

[6] J. Kwieciński, A. D. Martin, P. J. Sutton, *Phys. Rev.* **D46** (1992) 921,
K. Golec–Biernat, J. Kwieciński, A. D. Martin, P. J. Sutton, *Phys. Lett.* **B355** (1994) 220.

[7] H1 Collaboration, C. Adlof et al., *Nucl. Phys.*, **B 485** (1997) 3.

[8] A. J. Askew, D. Graundenz, J. Kwieciński, A. D. Martin, *Phys. Lett.* **B 338** (1994) 92.

[9] A. H. .Mueller, *Nucl.Phys.*, **B 18C** (1991) 125.
J. Phys., **G17** (1991) 1443.

[10] J. Kwieciński, A. D. Martin, P. J. Sutton, *Phys. Rev. D* **46**, (1992), 921,
Phys. Lett., **B287** (1992) 254.

[11] J. Kwieciński, A. D. Martin, P. J. Sutton, *Nucl. Phys. (Proc. Suppl.)*, **B29A** (1992) 67.

[12] J. Bartels, A. De Roeck, M. Loewe, *Z. Phys.* **C** (1992),
J. Bartels, M. Besancon, A. De Roeck, J. Kurzhöfer, Proc. of the DESY Workshop 'Physics at HERA. Ed. W.Buchmüller and G.Ingelman, Hamburg (1991) 203.

[13] J. Bartels, V. Del Duca, A. De Roeck, D. Graudenz, M. Wüsthoff, *preprint, DESY-96-36*,
J. Bartels, V. Del Duca, M. Wüsthoff, *preprint, DESY-96-220.*

[14] D. Graundez, PROJET 4.13 manual, *Comput. Phys. Comm.* **92** (1995) 65.

[15] G. Ingelman, LEPTO 6.3, unpublished manual, see also
G.Ingelman, *LEPTO 6.1 – The Lund Monte Carlo for deep inelastic lepton–nucleon scattering*, Proc. of the DESY Workshop 'Physics at HERA. Ed. W.Buchmüller and G.Ingelman. Hamburg (1991) 1366.

[16] K. Charchuła, G. Schuler and H. Spiesberger, *Comp. Phys. Comm.*, **81** (1994) 381.

[17] A. Kwiatkowski, H. Spiesberger and H. J. Möhring, *Comp. Phys. Comm.*, **69** (1992) 155.

[18] L. Lönnblad, *ARIADNE v. 4*, program and manual, *Comp.Phys.Comm.* **71** (1992) 15.

[19] G. Marchesini and B. R. Webber, *Nucl. Phys.* **B310** (1988) 461.

[20] T. Sjöstrand, *Comp. Phys. Comm.* **71**(1986) 347;
T. Sjöstrand and M. Bengtsson, *Comp. Phys. Comm.* **43**(1987) 367.

[21] R. Brun et al., GEANT3 User's Guide, CERN–DD/EE 84–1, Geneva (1987).

[22] H1 Collaboration, I. Abt et al., The H1 Detector at HERA, DESY-93-103.

[23] H. U. Bengtsson, T. Sjöstrand, *Comput. Phys. Commun.* **46** (1987) 43.

[24] N. H. Brook,A. De Roeck, A. T. Doyle, RAYPHOTON2.0, Proceedings of the Workshop Physics at HERA, vol.3, DESY (1992) p. 1453.

[25] G. Kramer, S. G. Salesch, *Phys. Lett.* **B317** (1993) 218,
S. G. Salesch, DESY 93-196 (1993),
G. Kramer, S. G. Salesch, *Phys. Lett.* **B333** (1994) 519.

[26] H1 Collaboration, S. Aid et al., *Z. Phys.* **C 70** (1996) 17.

[27] V. Blobel, *Proceedings of the "1984 CERN School of Computing", Aigublava, Catalonia,* Published by CERN, July 1985, pp. 88-127.

[28] G. D'Agostini, *Nucl. Instr. Meth.* **A362** (1995) 487.

[29] B. Efron, *The Annals of Statistics* **Vol. 7 No. 1** (1979) 1.

[30] J. G. Contreras, *PhD thesis* Dortmund University (1997).

[31] J. Bartels et al., *Phys. Lett.* **B384** (1996) 300.

[32] J. Kwieciński, S. C. Lang private comunication (paper in preparation).

[33] J. Kwieciński, C. A. M. Lewis private comunication (paper in preparation).

[34] S. Wölfle, talk presented at the 5th International Workshop on Deep Inelastic Scattering and QCD DIS'97, Chicago, USA, 14-18 April 1997.

[35] E. Mirkes, D. Zeppenfeld, *Phys. Lett.* **B380** (1996) 205.

Acknowledgments

I would like to thank Prof Albert De Roeck and Prof Jacek Turnau for guidance on the forward jet analysis. Without their support and encouragement this thesis would have never been written.

I am very grateful to Dr Krzysztof Golec–Biernat for introducing me to the theoretical aspects of low–x physics. If I have ever managed to understand some details of QCD, it is thanks to his didactic talents only.
I also thank him for careful reading and helping me with correcting the manuscript.

I do wish to thank Dr Mariusz Przybycień for his help in writing the unfolding code and for the discussions and support while solving numerous problems of the analysis.

I thank my colleagues from the Forward Jet Group, Dr Joachim Kurzhöfer and Dr Jesus Guillermo Contreras Nuño, for their help, cooperation and fruitful discussions on various issues of the analysis.

I am grateful to the Durham group: Prof Jan Kwieciński, Prof Alan Martin, Sabine Lang and Claire Lewis, for discussions on the theoretical aspects of the forward jet analysis and for providing me with the results of their calculations.

I thank Prof Krzysztof Rybicki, leader of the H1 Cracow Group, for his support and critical reading of the manuscript. I also acknowledge the help of all members of the Counter Group.

I would like to thank the DESY Directorate for financial support during my stay at DESY. I also thank the Polish State Committee for Scientific Research for their financial support (grant No. 2 P03B 129 10).

I am grateful to Mrs. Dorota Żenczykowska for correcting my written English.

Last but not least, I want to thank my parents and my husband Bogdan. Their contagious enthusiasm, support, continuous encouragement and patience have made this thesis possible.